

## Nucleation effects on cavitation about a sphere

Paul A. Brandner<sup>1</sup>, James A. Venning<sup>1,†</sup> and Bryce W. Pearce<sup>1</sup>

<sup>1</sup>University of Tasmania, Launceston, Tasmania, 7250, Australia

(Received 16 December 2021; revised 8 May 2022; accepted 24 May 2022)

The influence of nucleation on cavitation about a sphere from inception through to supercavitation at a transcritical Reynolds number of  $1.5 \times 10^6$  is investigated experimentally. Two extreme free-stream nuclei populations, deplete and abundant, were investigated. Unsteady surface pressures from two sensors on opposing sides of the sphere were acquired simultaneous with high-resolution high-speed photography at cavitation numbers between 1.0 and 0.3. High-resolution spectrograms derived from these measurements reveal principally bi-modal shedding in attached and detached regimes. Correlations between unsteady pressure measurements show the high modes to be axisymmetric and low modes asymmetric. Modal topology is also discerned from the high-speed imaging. The bi-modal shedding for lower cavitation numbers is driven by coupled re-entrant jet formation and upstream shockwave propagation. The attached regime is shown to have two sub-regimes. For the abundant case, the continuous supply of activated nuclei around the sphere periphery in the first bi-modal regime has the effect of driving the high symmetric mode preferentially over the asymmetric low mode compared with the deplete case. For the first bi-modal regime, frequencies were unaffected by nucleation changes although peak responses were centred at a cavitation number of about 0.8 for the deplete and 0.825 for the abundant. For the second attached regime, where cavity lengths are of the order of the sphere size, changes in nucleation altered frequencies and amplitudes of peak unsteady pressures. For the abundant case, the continuous nuclei supply significantly reduced coherence with modal peak amplitudes reduced by an order compared with the deplete case. Continuous nuclei activation increased the probability of the high mode over the low compared with the deplete case but to a lesser extent than the first regime. Nuclei activations also significantly reduced inter-cavity and cavity durations, but not growth and collapse phases, which increased modal frequencies compared with the deplete case. The second regime asymmetric low mode topology, for both nucleation cases, is shown to be alternate shedding of oblique vortices from diametrically opposing sides of the sphere similar to low Reynolds number shedding about spheres and other axisymmetric bluff bodies in single-phase flows.

† Email address for correspondence: [james.venning@utas.edu.au](mailto:james.venning@utas.edu.au)

**Key words:** multiphase flow, cavitation

---

## 1. Introduction

Cavitation inception and occurrence about axisymmetric bodies, including spheres and various headforms, has been widely studied since mid-last century (Lindgren & Johnsson 1966; Brennen 1969, 1970). More recently, Tassin Leger & Ceccio (1998) and Tassin Leger, Bernal & Ceccio (1998) have reported extensive experimental studies of liquid surface detachment and interfacial phenomena on spheres, headforms and hydrofoils. These have provided a richer understanding of cavitation inception and the association of viscous effects with cavity formation as summarised in the important monographs on the topic of cavitation by Brennen (1995) and Franc & Michel (2005).

Cavitation about a sphere is of interest as a canonical flow for both computational and experimental investigation. Such bodies of revolution may be tested in a water tunnel free from direct wall effects and have sufficient volume for inclusion of instrumentation. Recent contributions on cavitation, from inception through to supercavitation, about a sphere at a high (transcritical) Reynolds number have been made by Brandner *et al.* (2007*b*) and Brandner *et al.* (2010). It was found that at high cavitation numbers small-scale interfacial instabilities (identified as Kelvin–Helmholtz (K-H)) and turbulent transition of the overlying boundary layer were the main mechanism for cavity breakup and cloud formation. At intermediate cavitation numbers, cavity lengths allow the development of re-entrant jet phenomena (Callenaere *et al.* 2001), providing a mechanism for shedding of large-scale Kármán-type vortices similar to those for low mode shedding in single-phase subcritical flow (Sakamoto & Haniu 1990; Bakić & Perić 2005). These shedding modes are eliminated at low cavitation numbers with the onset of supercavitation. The shedding modes referred to here are physically axisymmetric vortex rings or asymmetric hairpin-like structures. A further study, with a particular focus on the dynamics of cloud cavitation, provided both additional evidence to attribute the small-scale shedding due to K-H instability and a new finding of coupled re-entrant jet/shockwave mechanisms for the classical cloud shedding instability in the case of a sphere (de Graaf, Brandner & Pearce 2017). At high cavitation number ( $\sigma > 0.9$ ) the shedding was found to be uni-modal with breakup driven by a small-scale K-H instability. However, for  $\sigma < 0.9$ , the cloud shedding was observed to be bi-modal (symmetric/asymmetric) in either an attached or detached regime ( $\sigma < 0.675$ ) depending on the cavity length. A re-entrant flow initiated breakup and a condensation shockwave, which propagated upstream, causing cavity collapse. More recently, modal decomposition of high-speed image data, based on the spectral proper orthogonal mode decomposition technique, has been applied to this complex flow to quantitatively identify the dominant shedding modes present. Three frequencies were found and both the shedding scale and type (symmetric/asymmetric) were identified from a single camera acquisition (Venning *et al.* 2018*a*). The technique was also extended to a dual camera acquisition giving more detailed information and significantly reducing the potential for ambiguity regarding the extracted shedding mode shapes (Venning, Pearce & Brandner 2021).

Subsequent to these experimental findings, results from numerical studies utilising compressible potential flow (Schmidt *et al.* 2008), large eddy (Pendar & Roohi 2018) and detached eddy (Cheng, Shao & Zhang 2019) simulations have been reported with each able to capture, to varying extents, some of the features of this complex two-phase unsteady flow. It will require further advancements and a substantial increase in computational

resources before high-fidelity simulation of all the physics involved, across the large range of both physical and temporal time scales, is realisable.

With cavitation occurrence, the similarity parameter generally used to characterise the dynamic flow conditions is the cavitation number. Cavitation inception will occur once the cavitation number is reduced below the incipient value which is dependent on the flow geometry and nuclei population. If the cavitation number is further reduced then the extent of the vapour cavity grows, and where associated with an immersed body (e.g. a sphere or lifting surface, etc) typically forms an attached partial cavity (cavity extent contained within the body length). With further  $\sigma$  reduction the cavity extends into the wake downstream from the body, then termed a supercavity (Franc & Michel 2005).

Inception of hydrodynamic cavitation in practical flows is invariably due to heterogeneous nucleation. These discrete sites of weakness, termed nuclei, are typically microbubbles either free in the liquid volume or volumes of gas trapped in or on adjacent surfaces. Depending on nuclei strength (which increases with reduction in size below 100  $\mu\text{m}$  Franc & Michel 2005), water can sustain tensions well below the saturated vapour pressure before vaporisation occurs (i.e. inception,  $\sigma_i$ , only occurring at a pressure  $< p_v$ ). Nuclei have been shown to control not only inception (Weitendorf 1981; Arndt & Keller 1992; Gindroz & Billet 1998; Arndt & Maines 2000) and affect developed partial cavitation (Briançon-Marjollet, Franc & Michel 1990) but also play an active role in the dynamics of shedding cavitation (de Graaf, Pearce & Brandner 2016; Venning *et al.* 2017, 2018b, 2021). Earlier investigations by Kawakami, Qin & Arndt (2003) and Kawakami *et al.* (2008), the latter presenting comparative results from three different facilities, identified the influence of dissolved gas level on the spectral content of cloud cavitation on a two-dimensional hydrofoil. Substantial differences in cavity shedding appearance and behaviour were noted between the results from the different facilities. Given the more recent findings noted above, it is likely that any variation of free-stream nuclei populations with dissolved gas level, both within and between the three facilities, may have contributed to the variation in the results, although nuclei populations were not measured in these experiments. In simulating cavitating flows the incorporation of nuclei has resulted in the capture of a number of features of inception and developed cavity dynamics as reported by Hsiao, Ma & Chahine (2017) and Ghahramani, Ström & Bensow (2021). An aim of the current work is to provide a high quality data set which may be useful to further improve these nuclei models and increase the fidelity of the physics captured within simulations.

As described above, the presence of nuclei up to a maximum size in a flow determine the tension which the liquid can withstand before breakdown or the formation of vapour bubbles occurs. This has led to descriptions of ‘strong’ through to ‘weak’ water depending on the level of tension or maximum size of nuclei present in the test circuit water flow (Arndt & Keller 2003). This effect is usually described as a ‘water quality’ aspect and is typically controlled by variation of the circuit dissolved air content. In practice this is difficult to achieve in a predictable manner and highly dependent on the individual facility architecture and operation (see, for example, Arndt & Maines 2000). This has led to significant differences in the inception data recorded in differing hydrodynamic experimental facilities, and within the same facility with differing operating conditions, which has been a longstanding issue (Lindgren & Johnsson 1966).

Alternatively, a limited number of water tunnels have been designed incorporating an enhanced capability to strictly manage the free-stream nuclei population (e.g. Briançon-Marjollet & Michel 1990; Briançon-Marjollet & Fréchou 1992; Brandner, Lecoffre & Walker 2007a). This is achieved by removal of all micron-sized bubbles and above by a combination of coalescence and buoyant separation and resorption at a low

dissolved air content (typically 30 % of saturation), and artificially injecting a controlled population of nuclei into the flow upstream of the working or test section. This technique effectively decouples the nuclei population from the dissolved air content if the latter is maintained within the limits of the facility's capacity to continuously remove all injected and cavitation generated nuclei, as demonstrated in a recent study by Khoo *et al.* (2020).

In the present work an experimental investigation has been undertaken on the effect of nuclei content on inception and developed cavitation about a sphere at a high (transcritical) Reynolds number in a cavitation tunnel. The facility used has the capability to independently control the free nuclei population and results are presented for two cases: nuclei deplete water and water seeded with a high nuclei concentration (referred to as the abundant case), maintaining all other flow conditions constant. The present study extends the earlier works by Brandner *et al.* (2010) and de Graaf *et al.* (2017) on cloud cavitation about a sphere in nuclei deplete flow to nuclei abundant flows. Simultaneous surface pressure measurement from sensors on both sides of the sphere, together with high-speed imaging, have gained further insights into the shedding physics, both in terms of spectra and the spatial character of the shedding behaviour.

## 2. Experimental approach

All experiments were carried out in the Australian Maritime College Cavitation Research Laboratory closed, recirculating, variable-pressure water tunnel (or cavitation tunnel). A schematic of the tunnel circuit is shown in [figure 1](#) with ancillaries relevant to the present work indicated. The tunnel test section is 0.6 m square by 2.6 m long, the nominal operating velocity and pressure ranges are 2 to 13 m s<sup>-1</sup> and 4 to 400 kPa absolute, respectively. The tunnel volume is 365 m<sup>3</sup> with demineralised water the working fluid. The circuit architecture is developed for continuous elimination of large volumes of injected incondensable gas and microbubbles, be they injected or created by cavitation. This is achieved through a combination of coalescence/buoyant separation in a downstream tank and dissolution via extended residence in a resorber. Ancillaries include a rapid degassing capability of 20 % of atmospheric saturation in 2 h. The circuit has low background noise and vibration levels through low velocities and isolation from the surrounding building and all noise-generating machinery. An array of microbubble injectors is located upstream of the honeycomb for homogeneously seeding the flow with cavitation nuclei of varying size and concentration. The combination of these capabilities enable cavitation experiments in flows with a predetermined dissolved gas constant and free-stream nuclei population.

The 150 mm diameter model sphere is sting mounted on the test section centreline ([figure 2](#)). Details of the model are shown in [figure 3](#). The sphere has a polyvinyl chloride (PVC) front section extending 120° from the front stagnation on which the cavitation forms and detaches. The stainless steel rear section, to which the sting is connected, contains two 2.5 mm diameter flush-mounted piezoelectric dynamic pressure sensors (PCB 105C02) located 125° from the front stagnation in a horizontal plane on the sphere centre. The two pressure sensors located on either side of the sphere allow determination of whether the cavity shedding is axisymmetric or asymmetric. The sensors were located to be within the cavitation shedding zone. The sensor locations are referred to as 'near side' and 'far side', with respect to the camera location, as shown in [figure 3](#).

The two test conditions of nuclei deplete and nuclei abundant were both achieved while operating the tunnel with the water dissolved oxygen content maintained at nominally 3 ppm. The measured deplete and abundant populations are shown in [figure 4](#) in four representations that may be used to characterise nuclei populations, i.e. cumulative (C) or non-cumulative (dC) concentration as a function of either critical tension or bubble

## Nucleation effects on cavitation about a sphere

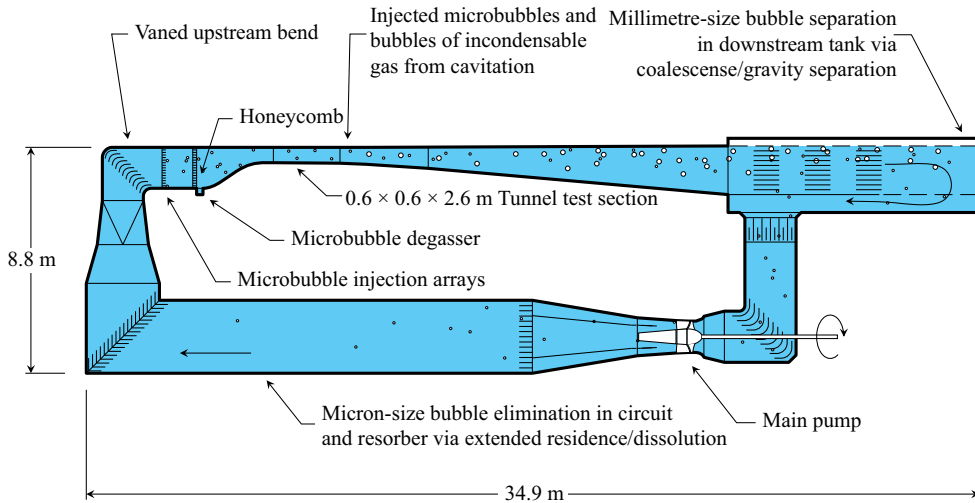


Figure 1. Schematic of the variable-pressure water tunnel showing circuit architecture for continuous removal of microbubbles or large volumes of injected incondensable gas and ancillaries for microbubble seeding and for degassing of water. Microbubbles may be either injected for modelling cavitation nucleation or generated by the cavitation itself.

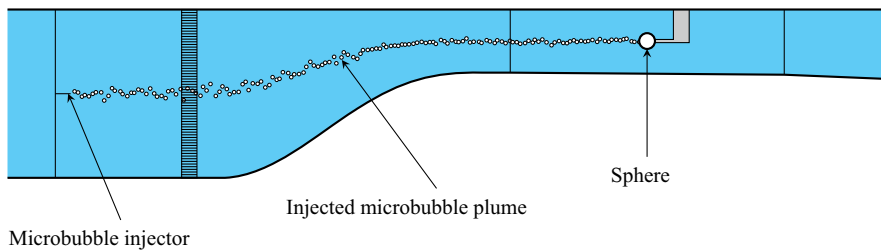


Figure 2. Schematic of the experimental arrangement in the test section. The sphere is positioned at mid-length on the test section centreline. For the abundant population case, nuclei are injected upstream of the inlet contraction at mid-height resulting in a plume of microbubbles on the test section centreline of about 80 mm diameter.

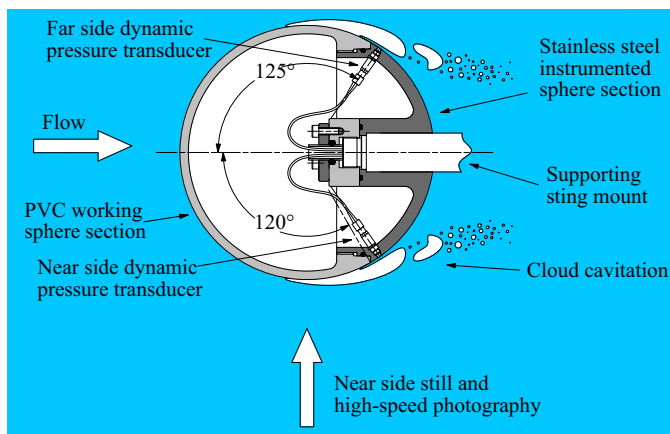


Figure 3. Top-down view of the sphere assembly. The flow is from left to right. Cameras image the cavitation from the bottom of the diagram (i.e. from the side of the test section).

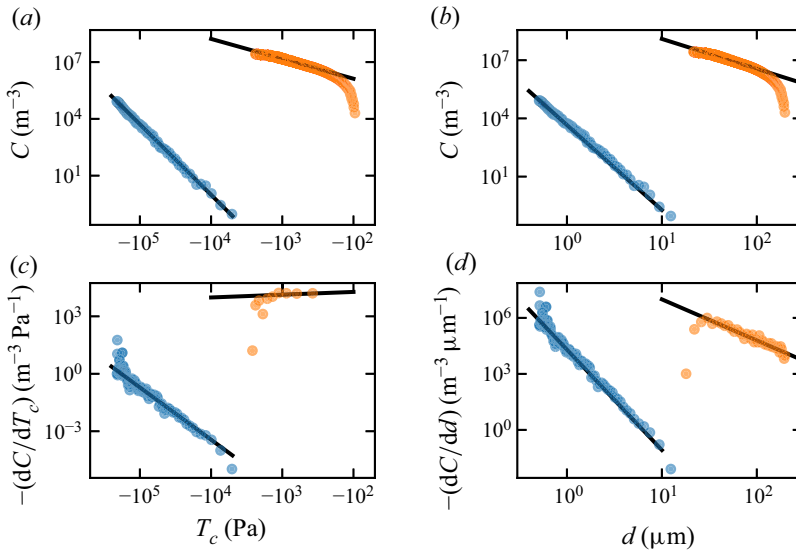


Figure 4. Background nuclei (blue) and injected (orange) size and concentration distributions. The background population was measured mechanically using a cavitation susceptibility meter, while the larger and more dense injected population was measured using Mie-scattering imaging. The data can be represented four ways as combinations of cumulative (a,b) or non-cumulative (c,d) populations as functions of tension (a,c) or diameter (b,d). The black lines are power-law fits to the data.

diameter at a particular free-stream pressure. Each representation is of use in the analysis of inception and nucleation in cavitating flows. The deplete population is measured directly as a cumulative concentration in critical tension via mechanical activation of the nuclei, whereas, the abundant population is measured optically in diameter at a given ambient pressure. How the deplete and abundant populations were achieved and measured is described in more detail below. The cumulative distribution is converted to non-cumulative by differentiation, or the reverse by integration. Conversion between critical tension and equivalent bubble diameter can be made from theoretical consideration of the stability of single bubble equilibrium or the Rayleigh–Plesset equation (Brennen 1995; Franc & Michel 2005). The critical pressure,  $p_c$  (so-called Blake threshold pressure), or tension,  $T_c$ , from a measured bubble diameter,  $d$ , and ambient pressure,  $p_\infty$ , assuming a fixed isothermal gas volume can be calculated from

$$T_c = p_c - p_v = -\sqrt{\frac{4}{27} \frac{(4S/d)^3}{p_\infty - p_v + 4S/d}}, \quad (2.1)$$

where  $p_v$  is the vapour pressure and  $S$  the surface tension. This equation can be rearranged into the following cubic that can be numerically solved for the equivalent bubble diameter at a particular ambient or initial pressure from  $T_c$ :

$$\left(\frac{d}{4S}\right)^3 (p_\infty - p_v) + \left(\frac{d}{4S}\right)^2 - \frac{4}{27(T_c)^2} = 0. \quad (2.2)$$

As noted in the introduction, for the deplete population, no nuclei were injected such that only the naturally occurring permanent background population remained. This population has been measured and shown to be practically inactive in higher cavitation numbers flows

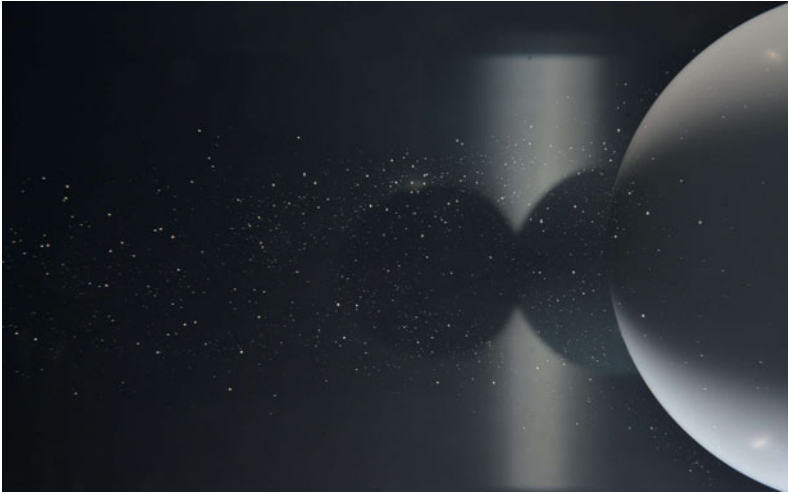


Figure 5. Photograph of the microbubble plume approaching the sphere (abundant case). The plume is approximately 80 mm in diameter.

such as the present experiment (Venning *et al.* 2018c), and more detailed evidence of this is provided in the current results. The background nuclei population are too small and sparse to be measured using optical techniques and have been measured using a cavitation susceptibility meter (CSM). Water sampled from the tunnel is passed through a venturi activating all nuclei with critical pressures greater than the throat pressure. Each activation is counted using an ultrasonic sensor. Variation of the throat pressure and flow rate measurement results in a cumulative distribution of concentration against critical pressure, as shown in the upper left plot of figure 4. The CSM used in the Cavitation Research Laboratory is described in Khoo *et al.* (2020). The background population has been measured in detail and found to obey a power-law relationship between cumulative concentration and critical pressure and to be invariant of normal tunnel operating conditions (Venning *et al.* 2018c; Khoo *et al.* 2020). Although the background nuclei are practically inactive for cavitating flow about the sphere, due to low critical pressure and concentration, there is a small probability that larger nuclei may still be activated, albeit rarely. Indeed it is these nuclei, or a remnant bubble, after filling and purging, that must be relied upon for initial inception in the nuclei deplete case.

For the nuclei abundant case, a single microbubble injector is deployed to seed the flow about the model sphere with nuclei. This is located on the tunnel centreline upstream of the honeycomb, as shown in figure 2, resulting in a plume of microbubbles on the test section centreline of about 80 mm diameter. A photograph of the plume is given in figure 5. A discussion on the streamtube required to be seeded depending on the nuclei population and cavitation number is provided below. The injector used generates a polydisperse microbubble population nominally less than 100  $\mu\text{m}$  diameter, a dominant size of 15  $\mu\text{m}$ , at a rate of  $10^6 \text{ s}^{-1}$  (Giosio, Pearce & Brandner 2016). The resulting population in the test section was measured using Mie-scattering imaging (MSI) (Damaschke, Nobach & Tropea 2002; Russell *et al.* 2020a,b), which utilises off-focus imaging of the spherical microbubbles illuminated with a coherent, polarised light source to determine the size of each bubble. The images were processed using a continuous wavelet transform (Brandner, Venning & Pearce 2018) to give the non-cumulative distribution in diameter for typical

test pressures ranging between 50 and 30 kPa, as shown in the upper right plot in [figure 4](#). The injected population may also be approximated with a power law for all but the larger sized, but low concentration, bubbles.

As noted above, for the background nuclei, being too small and sparse to be practically imaged, the measured critical tensions were converted to an equivalent diameter for the same ambient pressure under which the abundant population were measured enabling their direct comparison as shown in [figure 4](#). Indeed, as can be seen from [figure 4](#), the minimum microbubble diameter resolvable with the MSI is of about 10  $\mu\text{m}$  which is about the same as the maximum equivalent diameter of the background population. The CSM is able to resolve larger microbubble diameters up to about 80  $\mu\text{m}$  if present, however none were detected.

High-resolution photographs of the cavitation were captured with a Nikon DSLR D800 camera with a 60 mm lens (Nikkor, Japan) with a magnification factor of 21.3 px  $\text{mm}^{-1}$ . Lighting was provided by two stroboscopic lamps (Drello, Germany) placed symmetrically above and below the sphere. High-speed photography was captured with a HighSpeedStar 8 camera (LaVision, Germany) recording at 7000 frames per second for 3 s. Illumination was provided by two LED array lights. The high-speed photography was synchronised with the dynamic pressure measurements to allow correlation between pressure fluctuations and cavity dynamics. In order to discern the nature of the out-of-phase cavity shedding events, an additional set of high-speed images were acquired with two synchronised cameras for a cavitation number of 0.8, visualising both sides of the wake simultaneously. Images were acquired with two Phantom v2640 cameras each acquiring 2048  $\times$  1280 pixel images at 9900 frames per second. All imaging was acquired with the cameras located at the side of the test section.

The Reynolds number,  $Re = U_\infty D/\nu$ , was set at a fixed value of  $1.5 \times 10^6$  for this experiment, where  $D$  is the diameter of the sphere,  $U_\infty$  the free-stream velocity and  $\nu$  the kinematic viscosity of the water. The cavitation number,  $\sigma = 2(p_\infty - p_v)/\rho U_\infty^2$ , where  $p_\infty$  is the free-stream static pressure on the sphere centreline,  $p_v$  the vapour pressure of water and  $\rho$  the water density, which was varied from 1 to 0.3 corresponding to inception through to supercavitation. The pressure coefficient,  $C_p$ , is  $2p/\rho U_\infty^2$ . The viscosity, density and vapour pressure of the water were derived from real-time temperature measurements.

The unsteady pressure signals were recorded simultaneous with the high-speed imaging at 7 kHz for 3 s for  $\sigma$  values between 1 and 0.3 at 0.1 increments. Additional long series measurements of the unsteady pressures were made for spectral analysis for  $\sigma$  values between 1 and 0.3 at 0.025 increments. The signals were recorded at 1024 Hz, for 256 s at each cavitation number. These were decomposed with a Fourier transform using a Welch periodogram (Welch 1967) with Hanning windows. The length of each window was 1024 samples, or 1 s, with an overlap of 256 points between windows. This window length was chosen so that each window contained approximately 18 cycles of the expected dominant frequency. The power spectra from each window were then averaged to produce spectrograms of frequency content as a function of the cavitation number. These spectra obtained at each cavitation number increment then provide high-resolution spectrograms. The cross-power spectral density (CPSD) between the near and far pressure series was also estimated using the same Welch parameters. The phase difference between the two sides gives an indication of the state of symmetry as it varies with cavitation number.

The pressure time series were also analysed using the continuous wavelet transform (CWT), following the procedure of Torrence & Compo (1998). Here, the Morlet wavelet was correlated at various scales with the time series, allowing events in the surface pressure history to be isolated. Furthermore, the cross-wavelet transform (XWT)

(Grinsted, Moore & Jevrejeva 2004) was used with near-side and far-side pressure signals to identify the difference in phasing of structures on either side of the sphere.

### 3. Results

#### 3.1. Mean geometry and variation of cavity topology

A set of still images depicting the development of cloud cavitation about the sphere with reduction in  $\sigma$  from inception through to supercavitation for the nuclei deplete and abundant cases are shown in figure 6. Excerpts from the high-speed photography for both cases for  $\sigma$  values from 1.0 to 0.3 in 0.1 increments are available online as supplementary movie 1 available at <https://doi.org/10.1017/jfm.2022.511>. The general occurrence of cloud cavitation about a sphere for the present test conditions in the deplete case has been described by Brandner *et al.* (2010) and de Graaf *et al.* (2017), as reviewed in the introduction. The following discussion includes results on the differences in cavitation occurrence between the deplete and abundant nucleation cases as well as new findings on cavity topology for both cases.

Inception in both cases occurs at about  $\sigma = 1.0$  as the minimum value of  $C_p \approx -1.1$  for a transcritical Reynolds number (as defined by Achenbach 1972). For the deplete case, this was an intermittent process due to the lack of available nuclei. As noted above, inception in this case may be initiated due to a remnant bubble or from the background nuclei population which may require a period of time before a sufficiently weak nucleus is encountered. For the abundant case, there is a continuous supply of sufficiently weak nuclei such that inception is immediate once  $\sigma \approx -C_{p,min}$  (Franc & Michel 2005), which corresponds to a minimum pressure of vapour pressure.

The cavity leading edge or line of detachment in the deplete case is clearly defined and is associated with separation of the oncoming laminar boundary layer (Briançon-Marjollet *et al.* 1990). For the abundant case, the nuclei homogeneously dispersed in the free stream are activated at streamwise planes corresponding to the critical pressure of each nuclei (larger nuclei activating further upstream). Activated nuclei rapidly grow as discrete macroscopic cavitation bubbles with downstream advection. This discontinuous leading edge can then be defined in terms of the local streamwise void fraction. Continuous activation of nuclei and the subsequent growth and coalescence of cavitation bubbles leads to the formation of cavities of clustered or contiguous bubble volumes. Activated nuclei grow to maximum sizes of about 1 cm at area concentrations of order  $1 \text{ cm}^{-2}$ , both of which increase with decreasing cavitation number. The volumetric concentration of nuclei activations and the streamwise rate of increase of void fraction increases with decreasing  $\sigma$ . Cavities in the abundant case have a similar global extent to those in the deplete case, but with a locally lower void fraction. As described by Li & Ceccio (1996) and Brandner *et al.* (2010), it is the local three-dimensional flow about activated bubbles that breaks up the oncoming laminar boundary layer, preventing the formation of a continuous cavity leading edge and detachment line, as occurs for the deplete case.

At high cavitation numbers ( $\sigma \approx 1.0$  to 0.9) in the deplete case, the K-H instability in the separated laminar shear layer largely controls transition to turbulence and cavity breakup and condensation. Although developed cavitation bubbles tend to merge for the abundant case, the cavity breakup and condensation, with downstream pressure recovery, is of a discrete nature (see online movie 1). This behaviour can be attributed in part to discrete bubble collapse but also to the three-dimensional flows about each activated bubble that initially breakup the upstream laminar boundary layer. Both effects contribute to larger-scale vortical structures in the wake of the condensed cavity in the abundant case

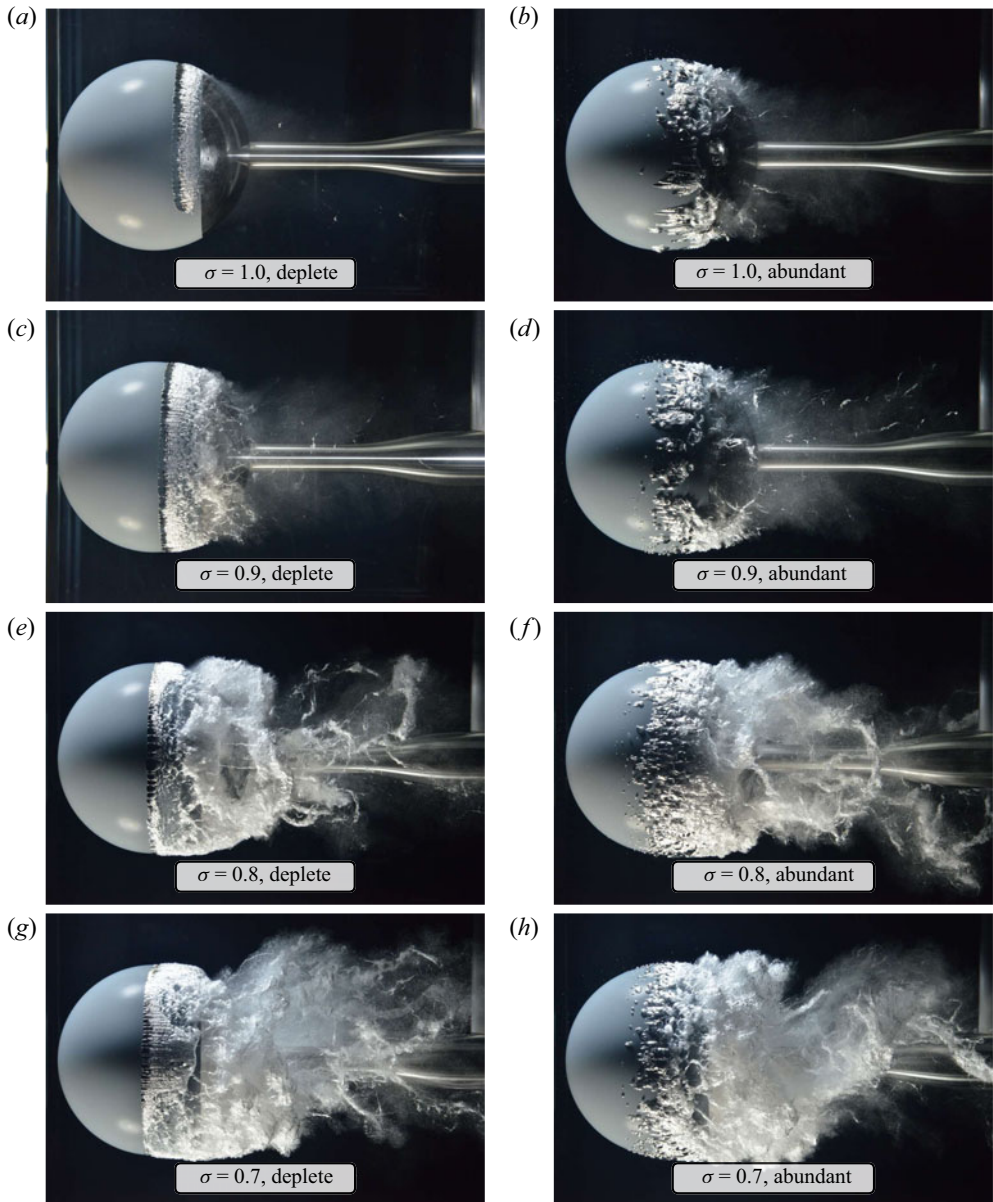


Figure 6. For caption see next page.

compared with the deplete case where interfacial instabilities are of a much finer scale. The cavity extent at these higher  $\sigma$  values, both upstream and downstream, is greater for the abundant case due to earlier nuclei activation upstream of the detachment line for the deplete case. Additionally, the bubbles collapse further downstream in the abundant case, condensing as the pressure recovers in the wake.

With reduction of  $\sigma$  below 0.9 cavity lengths just become sufficient in both deplete and abundant cases for re-entrant flow and coherent shedding to begin to develop. The high-speed imaging and measured spectra show the shedding to be uni-modal and of

Nucleation effects on cavitation about a sphere

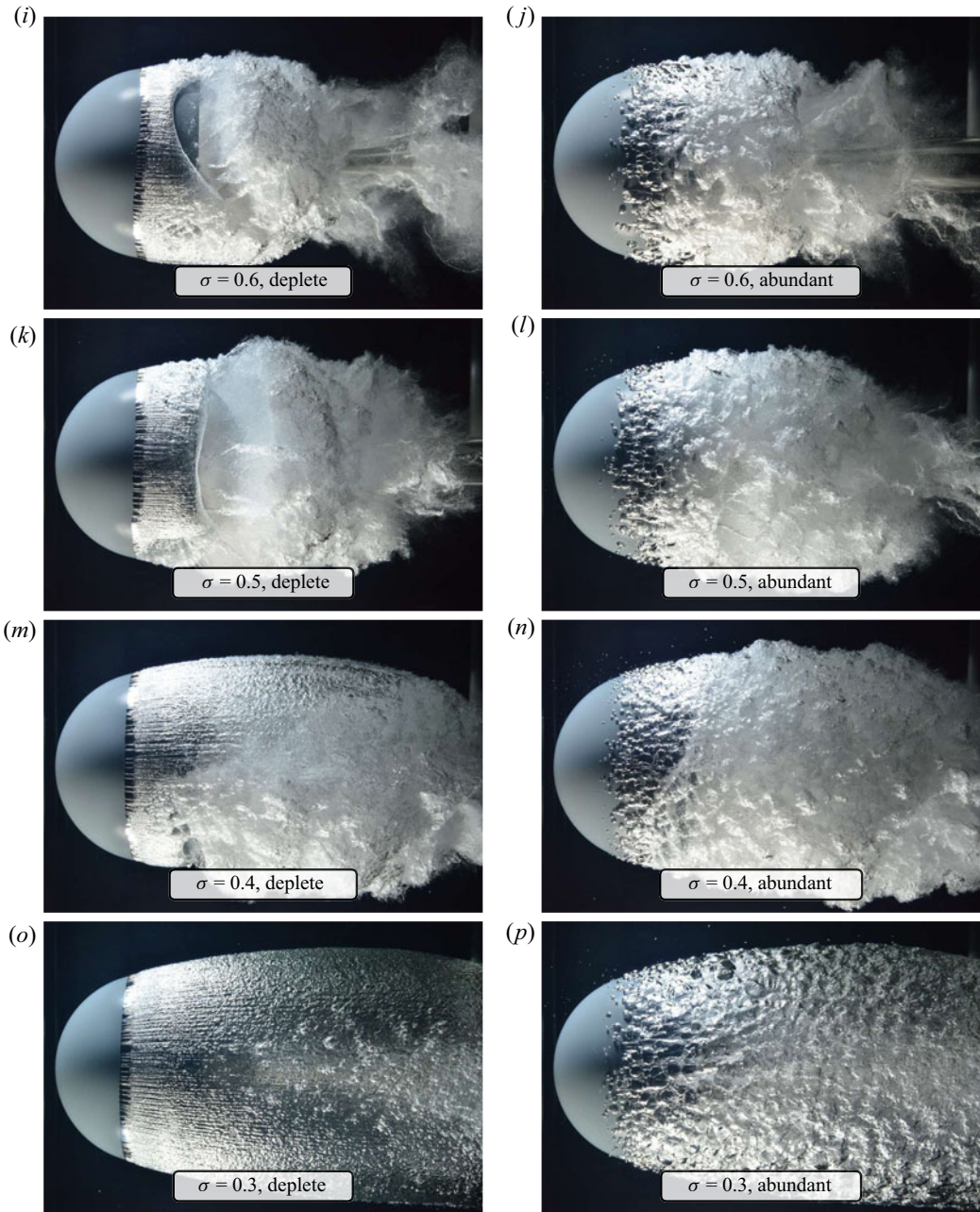


Figure 6 (contd). Cavitation development with cavitation number reduction. The left column (*a,c,e,g,i,k,m,o*) is with water deplete of nuclei, and photographs of the abundantly seeded cases are in the right column (*b,d,f,h,l,n,p*).

axisymmetric character, as discussed in § 1. Large-scale cavity shedding ensues for  $\sigma$  values between approximately 0.8 and 0.6 where it becomes predominately bi-modal for the abundant as well as the deplete case. As discussed earlier, these are attributed to axisymmetric and asymmetric modes in attached and detached regimes. The differences in nucleation affect both frequencies and amplitudes of surface pressures which are analysed

in detail below. This shedding is driven by coupled re-entrant jet formation and upstream shockwave propagation that at its most energetic creates large-scale circumferential cavity extinction with subsequent re-nucleation. In the deplete case as there are no free-stream nuclei these must be supplied by remnant bubbles from cavity extinction or from surface nuclei. Although detailed investigations have not been carried out to definitively demonstrate the source of nuclei, high-resolution photography and high-speed imaging suggest the former to be the case at least for this PVC sphere. Russell & Brandner (2021) studied coherent cloud cavitation about a NACA 16 hydrofoil where shockwave-driven large-scale extinction and re-nucleation occurred for each cycle. They showed that nuclei were provided from the condensation and breakup of the previously shed cavities. Ram, Agarwal & Katz (2020) showed similar phenomena associated with the breakup of incipient cavities in adverse pressure gradients and further showed how remnant bubbles can be transported upstream by reverse flow or indeed buoyancy alone.

For the abundant case with a continuous supply of nuclei, the overall nature of the large-scale shedding is similar although the cavities are discontinuous as evident from the still and high-speed photography. Re-entrant jets develop as the cavities grow and with fluid accumulation and eventual penetration of the outer cavity surface shockwaves are initiated in a similar process to the deplete case. As the cavity is composed of discrete bubbles, the shockwave can be seen to propagate upstream in a discontinuous manner. Unlike the deplete case, shockwaves rarely cause large-scale extinction due to the continuous nuclei supply, particularly as  $\sigma$  is reduced. At the lower  $\sigma$  values bi-modal shedding in the detached regime persists but at decreasing frequencies until the supercavitation regime forms at  $\sigma \approx 0.3$ .

The global cavity geometry is generally similar for all  $\sigma$  values and comparisons of basic geometric and kinematic properties can be derived from the still and high-speed photography. Measurements of the cavity upstream extent for the deplete and abundant cases and comparisons with basic theory are shown in figure 7. The angle of cavity detachment,  $\theta$ , measured from the front stagnation point for the deplete case has been derived from the still photography measured using only the two detachment locations on the vertical centre plane to avoid image distortion effects. Previous measurements of cavity detachment angle, in the deplete case, by Brandner *et al.* (2010) and de Graaf *et al.* (2017) for an arbitrary point gave a linear relationship between  $\theta$  and  $\sigma$ . The present measurement shows that by eliminating distortion this relation is slightly nonlinear. The cavity detachment angle for the deplete flow appears to occur some 25 to 30° downstream of the angle at which the surface  $C_p = -\sigma$  as derived from single-phase inviscid theory ( $\theta = \arccos \frac{1}{3} \sqrt{5 - 4\sigma}$ ). This difference is in part attributable to boundary layer and surface tension effects but also that the pressure distribution on a cavitating sphere will be different from that for single-phase inviscid theory. For the abundant case, the angle at which activated nuclei first become visible is plotted. These were extracted from high-speed photography and defined as the angle at which the pixel intensity fluctuations increased above the background noise level. This location has a weak dependence on the camera magnification and lighting. More magnification would result in bubbles being visualised earlier in their growth, thus reducing the angle. These points are some 5 to 10° downstream of the angle at which  $C_p = -\sigma$  as derived from single-phase inviscid theory. These curves would be expected to converge for high  $\sigma$  values as the cavity volumes decrease except that, as noted above, the minimum  $C_p$  for a transcritical Reynolds number is about 0.1 less than the inviscid solution which explains, in part, the lack of close convergence near inception. Brennen (1969) obtained an inviscid solution for cavitating flow about a sphere for cavitation numbers between 0.6 and 0.2. This range corresponds

## Nucleation effects on cavitation about a sphere

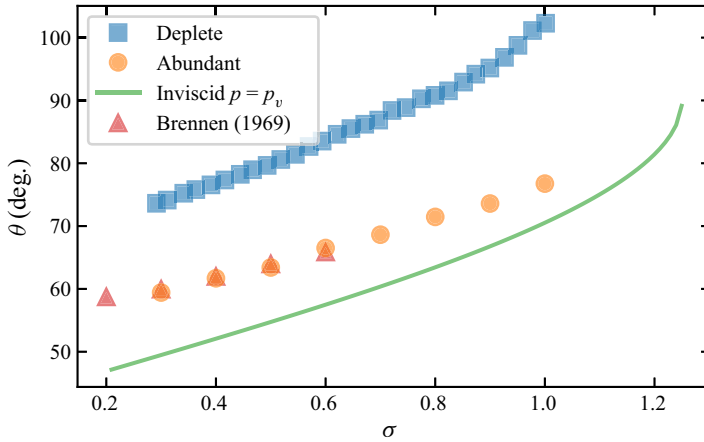


Figure 7. The location of the detachment line for the unseeded case (blue) as a function of cavitation number. The activation angle for the nucleated case is in orange. The inviscid solution for the location of where the pressure equals the vapour pressure is given in green, ignoring the presence of the cavity. The computational solution from Brennen (1969) including the cavity is also included in red. All angles are measured from the front stagnation point.

closely with the detached regime observed in experiments (de Graaf *et al.* 2017) where cavity closure occurs downstream of the sphere for which solutions could be obtained for the method used by Brennen. The imaging and surface pressure spectra obtained in the present work also show the detached regime to commence at cavitation numbers between about 0.6 and 0.7. The results obtained by Brennen are included in figure 7 and these show close agreement with the angle at which the activated nuclei first become visible in the abundant case. This result suggests that the boundary layer, being relatively thin compared with the diameter, has little effect and that the real flow is closely modelled using inviscid theory with the cavity included.

The differences between the deplete detachment line and the abundant activation line can be explained by consideration of the combined effects of boundary layer separation and discrete bubble activations (Li & Ceccio 1996; Tassin Leger & Ceccio 1998). As noted by Arakeri & Acosta (1973) and Arakeri (1975), the cavity detachment without nuclei is associated with an upstream laminar boundary layer separation. For the boundary layer to separate, an adverse pressure gradient must exist upstream of the cavity detachment line, such that the liquid upstream is at a lower pressure and in a state of metastable tension as discussed by Briançon-Marjollet *et al.* (1990), Tassin Leger & Ceccio (1998). For the abundant case, where there are free nuclei, these are activated in this region of tension upstream of the unperturbed detachment line. With sufficient rates of activation, the detachment line approaches the inviscid solution of Brennen (1969), hence the excellent agreement as shown in figure 7.

### 3.2. Nuclei activation rates

Once the nuclei are activated and visible their advection speed may be measured from the high-speed photography and comparisons made with the inviscid velocity,  $U = U_\infty \sqrt{\sigma + 1}$ , that occurs in the flow where  $C_p = -\sigma$  for the abundant flow case. For the deplete case where there are no active nuclei, this velocity is the inviscid cavity surface speed. The measured activated bubble velocities and the inviscid velocity where  $C_p = -\sigma$  are shown in figure 8. The bubble advection velocities are all within about 10% of the

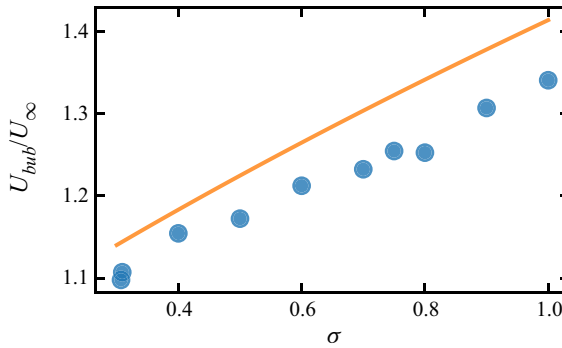


Figure 8. Bubble velocity ( $U_{bub}$ ) at the activation point as a function of the cavitation number for the nucleated cases. Also included in orange is the inviscid velocity found from theory as  $\sqrt{\sigma + 1}$ .

inviscid value. This difference may in part be attributed to the bubbles not being on the surface but possibly also due to the flow modification as a result of bubble growth and their finite size.

High-speed imaging of the activated nuclei can also be used to measure the nucleation rate at each  $\sigma$  and analyses performed to test how well these can be reconciled with the measured nuclei populations. Assuming the flow about the sphere is unaffected by the presence of cavitation, at least for the higher  $\sigma$  values, inviscid theory may be used to estimate nucleation rates from the measured nuclei populations. These rates can then be compared with those derived from the high-speed imaging.

For single-phase inviscid flow about a sphere, the minimum pressure for any streamline occurs on the spanwise plane at the origin ( $x = 0$ , in cylindrical polar coordinates as defined in figure 9). This plane can then be considered for estimating the nuclei activation rate for a particular  $\sigma$  value, as shown in figure 9. The pressure at this plane is given from inviscid theory as

$$c_p = 2 \frac{p_0 - p_{\infty}}{\rho U_{\infty}^2} = -\frac{a^3}{r^3} - \frac{1}{4} \frac{a^6}{r^6}. \tag{3.1}$$

Which can be converted to tension,  $T$ , through the definitions of the tension,  $T = p - p_v$ , and the cavitation number  $\sigma = 2(p - p_v)/\rho U_{\infty}^2$ . The tension, therefore, as a function of radial coordinate,  $r$ , is

$$T_0 = p_0 - p_v = \frac{1}{2} \rho U_{\infty}^2 \left( \sigma - \left(\frac{a}{r}\right)^3 - \frac{1}{4} \left(\frac{a}{r}\right)^6 \right). \tag{3.2}$$

This equation can be transposed to give the radial coordinate as a function of tension,

$$\left. \begin{aligned} \frac{r}{a} &= k^{-1/3}, \\ k &= -2 + 2 \sqrt{1 + \sigma - \frac{T}{\frac{1}{2} \rho U_{\infty}^2}}. \end{aligned} \right\} \tag{3.3}$$

This equation can be used to derive the streamtube of opportunity which encapsulates all streamlines that will be exposed to tensions equal to, or less than, zero, or equivalently, static pressures equal to, or less than, vapour pressure. Setting  $T = 0$  in (3.3) provides the

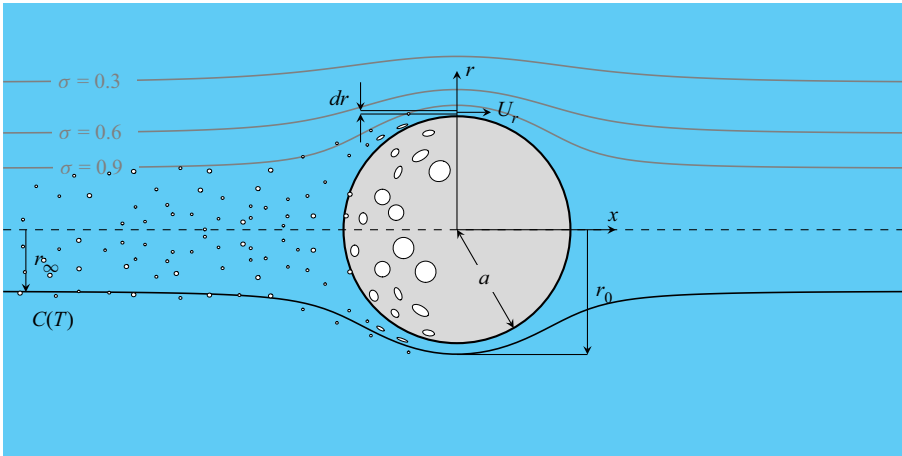


Figure 9. Coordinate system for the flow about a sphere. The streamtubes of opportunity ( $T = 0$ ) for selected cavitation numbers are indicated in grey.

radial coordinate at the origin at which vapour pressure occurs as a function of  $\sigma$ ,

$$\frac{r_0}{a} = \frac{1}{\sqrt[3]{2(\sqrt{\sigma + 1} - 1)}}. \quad (3.4)$$

The upstream radius of this streamtube is found by equating the streamfunction and finding the limit as the streamwise coordinate goes to infinity, that is, far upstream

$$\frac{r_\infty}{a} = \frac{r_0}{a} \sqrt{3 - 2\sqrt{\sigma + 1}}. \quad (3.5)$$

Streamlines defining the streamtubes of opportunity for selected  $\sigma$  values are shown in figure 9 and the streamtube radii at the origin and upstream as a function of  $\sigma$  are shown in figure 10. As noted above, this analysis is only justifiable for high  $\sigma$  values where the flow is least modified by the cavitation. Also noted earlier, the seeded plume for the nuclei abundant case is about 80 mm diameter, or about  $r_\infty/a = 0.5$ , and from figure 10 it can be seen that this is sufficient for the larger  $\sigma$  values. For  $\sigma$  values below 0.8 to 0.9, the curve shown in figure 10 indicates a much larger plume is required to seed the streamtube of opportunity. Although as discussed, this analysis is no longer justifiable with cavity volumes becoming large compared with the sphere volume such that the bulk flow will be significantly modified. It is arguable that the upstream diameter of the streamtube of opportunity will be significantly smaller than the single-phase result shown in figure 10, but it remains possible that the streamtube of opportunity for the lower  $\sigma$  values is not fully seeded. It is also worth noting that the radius of the streamtube of opportunity at the origin for the higher  $\sigma$  values only extends some 10% of the sphere radius beyond the surface, which is of the order of typical activated bubble sizes.

Nuclei transport in inviscid or viscous flows involves several forces demonstrated in recent examples of one-way coupled Lagrangian analyses by Hsiao, Ma & Chahine (2018), Chen *et al.* (2019), Beelen & van Rijsbergen (2018), Paul, Venning & Brandner (2021). Nevertheless, some insight can be gained into activated nuclei sizes and rates from an albeit simple analysis assuming ideal nuclei advection given the small sizes involved.

A closed-form expression for the nuclei activation rate for a single tension and cavitation number can be derived using the non-cumulative nuclei distribution in tension ( $-dC/dT$ ).

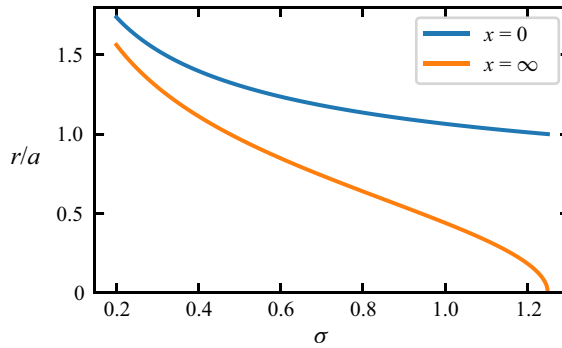


Figure 10. Radius of the streamtube of opportunity at the sphere (blue) and far upstream (orange).

The activation rate is here defined as the number of nuclei activations per unit time, and has the physical units of ‘per second’. The activation rate through a differential streamtube for a single tension is the product of the concentration for that tension and the differential flow rate. The total activation rate for that tension is then the integral of all differential streamtubes with tensions less than or equal to the tension in question,

$$\begin{aligned}
 \frac{dA}{dT} &= -\frac{dC}{dT} \int_a^{r_0(T)} U_r 2\pi r \, dr \\
 &= -\frac{dC}{dT} 2\pi U_\infty \int_a^{ak^{-1/3}} r \left( 1 + \frac{a^3}{2r^3} \right) dr \\
 &= -\frac{dC}{dT} \pi U_\infty a^2 (k^{-2/3} - k^{1/3}), \tag{3.6}
 \end{aligned}$$

where  $T$  and  $\sigma$  are encapsulated within  $k$ . By choosing a single tension the concentration term ( $-dC/dT$ ) is constant and can be excluded from the integration, the limits of integration are from the sphere surface to the radius where the tension is equal to the value chosen  $r_0(T)$ . Equation (3.6) may then be evaluated for all measured tensions for both the deplete and abundant nuclei populations, for the higher  $\sigma$  values, as shown in figure 11. Here the activation rates per unit tension have been converted to rates per unit diameter using (2.2). For the deplete case, the activation rates are small in comparison with the abundant case as expected and biased to the small nuclei sizes, as low as 5  $\mu\text{m}$ , where concentrations are much higher. This plot also shows the nonlinear increase in activation rates with decreasing  $\sigma$  again due to smaller nuclei with higher concentrations becoming susceptible. For the abundant flow, the plots are truncated at 18  $\mu\text{m}$  reflecting the lower bound of the MSI measurement. Here the rates are some  $10^6$  times greater with similar trends but less increase with decreasing  $\sigma$  due to the distribution not varying with tension or diameter as greatly as for the deplete case.

While (3.6) is useful in showing the dependencies involved to estimate the total nuclei activation rate its closed-form integration is cumbersome. Alternatively, the total rate may be numerically integrated directly by including the cumulative nuclei distribution  $C(T)$  in tension (or diameter) in the integration in a similar way as for (3.6) but integrating across

## Nucleation effects on cavitation about a sphere

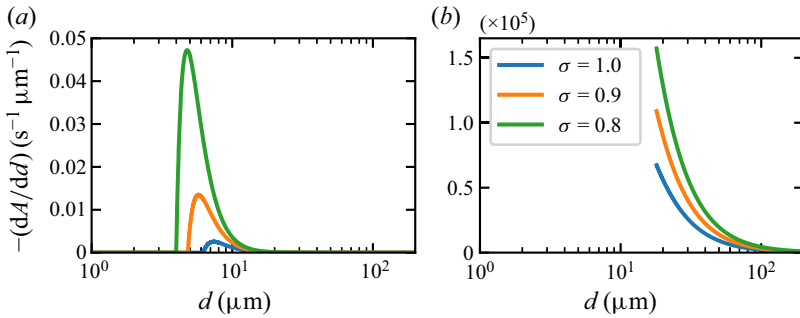


Figure 11. Activation rate per unit diameter as a function of bubble diameter from (3.6 and 2.2). Plot (a) is with the deplete nuclei population, and (b) is with the abundant. Note that there are six orders of magnitude difference between the vertical scales of the two figures.

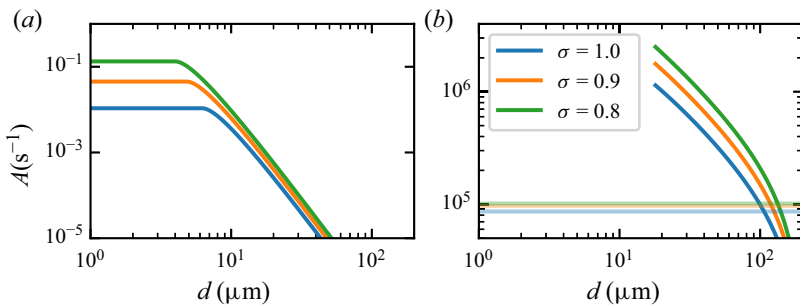


Figure 12. Total nuclei activation rate about a sphere for deplete (a) and abundant (b) free-stream nuclei levels. The horizontal lines indicate the measured activation rate from the high-speed videos.

all differential streamtubes with tensions less than zero,

$$\begin{aligned}
 A &= \int_a^{r_0} 2\pi r U_r C(T(r)) dr \\
 &= 2\pi U_\infty \int_a^{r_0} r \left(1 + \frac{a^3}{2r^3}\right) C(T(r)) dr.
 \end{aligned} \tag{3.7}$$

The results from (3.7) are shown in figure 12 as a cumulative plot starting from the largest nuclei. For the nuclei deplete case (left), the rates increase as a power law reflecting the deplete nuclei distribution. The curves reach a constant value at the smallest nuclei that can be activated for each  $\sigma$  which is about  $4 \mu\text{m}$  for the  $\sigma = 0.8$  case. In all cases the estimated total activation rates are small and are of the same order of magnitude observed in the experiments (this is a qualitative estimation since the interval between activations is some 10 times longer than the duration of the high-speed video recordings, precluding the calculation of an activation rate). As discussed in § 3.1, at high cavitation numbers it may take several minutes for a transient activation or inception to occur.

For the nuclei abundant case, the nuclei activation rates measured from the high-speed photography are included as horizontal lines in figure 12(b). These are total measurements across all nuclei sizes as the initial size before activation could not be measured. The growing microbubbles were counted manually in the video frames. Each activation was tagged and tracked with downstream advection ensuring double counting did not occur. The activation rate was relatively constant with  $\sigma$ , increasing from about  $0.86 \times 10^5 \text{ s}^{-1}$

at  $\sigma = 1.0$  to  $1.02 \times 10^5 \text{ s}^{-1}$  at  $\sigma = 0.8$ . The estimated activation rates are some one order of magnitude greater than those actually observed.

There are several assumptions to which these differences may be attributed. The inviscid minimum pressure coefficient of  $-1.25$  is lower than the value for the finite Reynolds number tested which, as noted above, is actually about  $-1.1$ . Although only large cavitation numbers, where cavity volumes are small, are considered, the presence of cavitation will further alter the pressure distribution from the inviscid case. The boundary layer, although thin, has not been accounted for and the decreased mass/nuclei flux would also reduce the activation rate compared with the pure inviscid case.

In the present analysis the critical spanwise plane at the origin, at which the inviscid minimum pressure occurs, is used to calculate the number of activated nuclei. Whereas in the real flow, larger nuclei will be activated at planes upstream of the minimum and these growing bubbles locally affect the flow. That is, for the present analysis, no interaction or coupling between phases is assumed. This concept is discussed by Franc & Michel (2005) and Lecoffre (1999) and relates to flows in which negative pressures occur such that once vapour bubbles develop, with effectively vapour pressure internally and at the surface, then at each bubble surface local pressures are raised from the single-phase negative pressures to vapour pressure. Furthermore, they explain that this effect can lead to a condition of saturation where an increase in the nuclei concentration produces no further increase in activation rate. Although local, these effects are distributed and introduce the potential for suppression of further nuclei activation and bubble-bubble interactions. Given that the thickness of the streamtube of opportunity about the sphere is of the order of the size of the cavitation bubbles this effect could be significant.

Finally, if all forces acting on the nuclei are accounted for, larger nuclei may not be carried ideally on the fluid streamlines but be deviated by pressure gradients and other effects. This phenomena known as ‘screening’ (Liu, Kuhn de Chizelle & Brennen 1993; Beelen & van Rijsbergen 2018; Hsiao *et al.* 2018; Chen *et al.* 2019; Paul *et al.* 2021) may lead to nuclei being transported from the inside to the outside of the streamtube of opportunity reducing the number of activations about the sphere compared with the potential available nuclei in the streamtube upstream. Liu *et al.* (1993) considered the screening problem for an axisymmetric headform and used potential flow about a sphere to derive an analytical model. Their results showed that screening, boundary layer and size effects can account for a reduction in activation rates of an order of magnitude. Although ultimately they showed that taking these effects in account predicted activation rates were one order of magnitude greater than those observed experimentally. Paul *et al.* (2021) considered nuclei transport about a sphere and showed that screening and other effects are small. These results would imply that the order of magnitude differences between predicted and observed results is most likely due to two-way coupling between the disperse and continuous phases. That is, as described above, activated finite growing bubbles eliminate local tension and, hence, suppress activation rates below expected values such that the activation rate has reached saturation.

### 3.3. Unsteady surface pressure and high-speed imaging

The standard deviation of the measured unsteady pressures from the near and far sensors, for the deplete and abundant nucleation cases, for all  $\sigma$  values are shown in figure 13. The near and far results show nominally the same amplitudes and trends as expected due to symmetry. The variation of amplitudes reflect the intensity and location of the shedding. For the deplete case at high  $\sigma$  values, the intensity is relatively low due to short cavity breakup driven by small-scale interfacial instabilities. The intensity increases rapidly with

### Nucleation effects on cavitation about a sphere

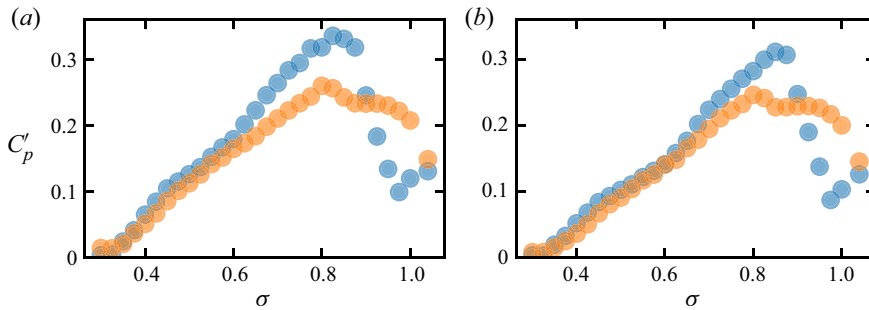


Figure 13. The effect of free-stream nucleation, cavitation number and pressure sensor location on the magnitude of the pressure fluctuations. The near sensor is in (a) and the far is in (b). The blue is using water deplete of nuclei, and the orange is with abundant nuclei injection.

$\sigma$  reduction as cavity lengths grow and the re-entrant jet instability develops. A maximum is reached within the attached shedding regime at about  $\sigma = 0.85$  which is attributable to the nature of the shedding as well as the proximity of the re-entrant jet location or shedding zone moving over the sensor location. Beyond the maximum, the amplitude reduces in a linear trend with reducing  $\sigma$  through the detached regime, where re-entrant jet formation is off-body. The standard deviation ultimately reaching zero with the formation of supercavitation where any unsteady flow occurs well downstream.

For the nuclei abundant case at high  $\sigma$  values, the amplitude increases immediately after inception to values much greater than the deplete case due to the unsteadiness created by continuous nuclei activation and collapse. For  $0.65 < \sigma < 0.9$ , corresponding to the attached shedding regime, amplitudes are reduced by about 10–20%. This reduction is due to the continuous nuclei activation breaking up or reducing the intensity and coherence of the large-scale shedding that would otherwise occur in the deplete case. As discussed in § 1, for the deplete case when the shedding is most energetic, the coupled re-entrant jet and shockwave formation lead to large-scale cavity extinction. That is, large regions of the flow may oscillate between 0–100% void fraction. For the abundant case where there is continuous nuclei activation and bubble growth, the flow does not reach such extremes, hence the reduction in amplitude in the attached regime. With reduction of  $\sigma$  into the detached and supercavitation regimes where shedding is moved downstream, differences in nucleation have a significantly reduced effect and amplitudes of the standard deviation for the two cases tend to converge.

The power spectral density (PSD) and CPSD of the near and far unsteady pressures, for deplete and abundant cases, are presented as spectrograms of cavitation number in figures 14 and 15, respectively, derived as described in § 2. Here the Strouhal number has been defined as  $St = fD/U_\infty$ . The amplitude scales of the power spectrograms in figure 14 are the same for deplete and abundant cases to show the relative magnitude of response of the various modes. The amplitude of the CPSD or coherence in figures 15 are also the same for each nucleation condition, but also coloured to show the phase angle between the near and far pressure signals.

In both cases just after inception for  $0.9 < \sigma < 1.0$  there is a uni-modal response in the frequency range  $0.25 < St < 0.50$ . For the deplete case, as discussed above, cavity breakup is driven by small-scale interfacial instabilities that lead to roll-up of larger-scale vortices shed within the frequency range noted above. This phenomena can be seen from the high-speed imaging in the supplementary material for  $\sigma = 0.90$  (see supplementary movie 1). The unsteady pressures show moderate coherence and to be out-of-phase which

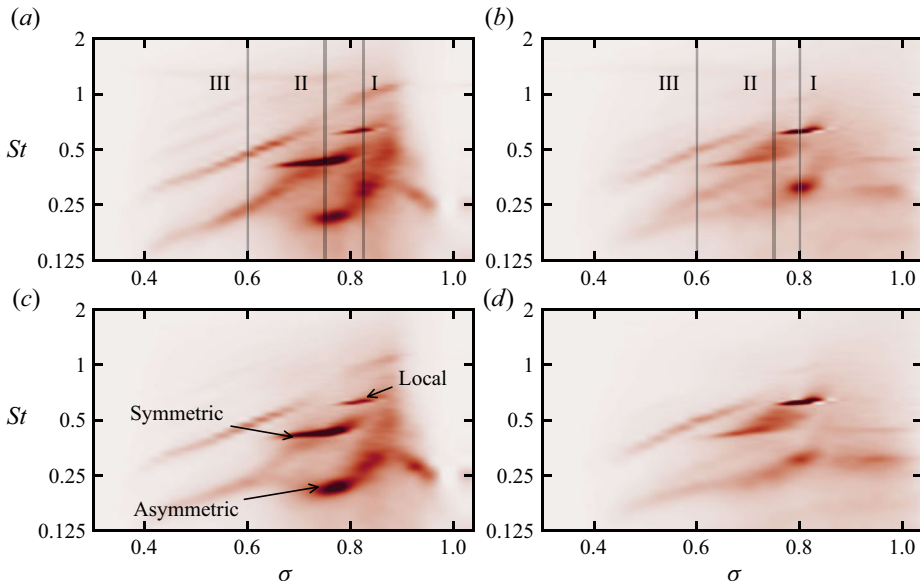


Figure 14. Spectrograms showing the cavitation dynamics as a function of the cavitation number. The influence of water quality is shown by comparing the *(a,c)* figures for the deplete case to the *(b,d)* figures with abundant nuclei injection. The *(a,b)* corresponds to the near pressure tap, while the *(c,d)* is the far. Neither the spectra nor the initial data have been normalised to enable a direct comparison. The vertical lines indicate the nominal positions of the three different shedding regimes.

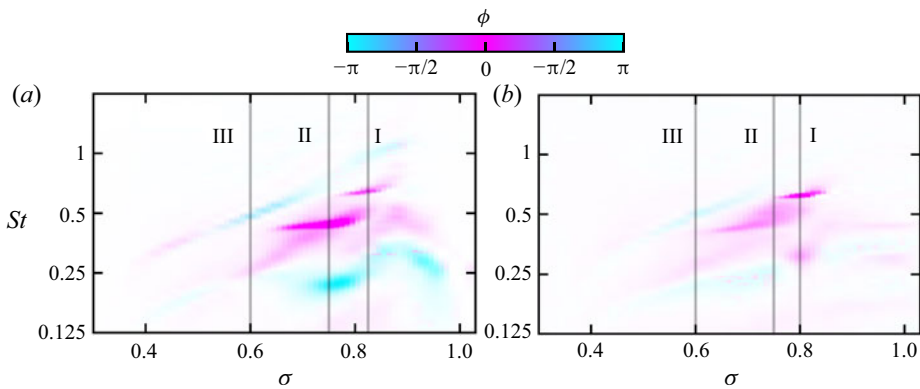


Figure 15. Phase difference of the CPSD between the two pressure sensors as a function of cavitation number. The phase is given by the colour, and the power sets the transparency. The flow is deplete of nuclei in *(a)* and abundant in *(b)*. The vertical lines indicate the three different shedding regimes.

could be attributed to the random nature of the local shedding. For the abundant case, continuous nuclei activation at close circumferential spacing around the sphere leads to contiguous cavity growth and downstream collapse. The discontinuous bubble or cavity collapse events appear to initiate local shockwave phenomena that momentarily propagate upstream contiguously. That is, there appears to be a dynamic equilibrium between downstream advection of growing/collapsing bubbles and upstream propagation of contiguous shockwaves from local distributed collapse events. In this case the unsteady pressures show weak coherence.

Regime	Deplete		Abundant	
I	$\sigma = 0.825$	$f_{dL}^I = 0.30, f_{dH}^I = 0.64$	$\sigma = 0.800$	$f_{aL}^I = 0.31, f_{aH}^I = 0.63$
II	$\sigma = 0.750$	$f_{dL}^{II} = 0.21, f_{dH}^{II} = 0.43$	$\sigma = 0.750$	$f_{aL}^{II} = 0.27, f_{aH}^{II} = 0.51$
III	$\sigma = 0.600$	$f_{dL}^{III} = 0.24, f_{dH}^{III} = 0.48$	$\sigma = 0.600$	$f_{aL}^{III} = 0.22, f_{aH}^{III} = 0.51$

Table 1. Strouhal number for each of the shedding modes in each cavitation regime. For each regime, I, II and III, there are two shedding frequencies, indicated by ‘L’ for the low-frequency mode and ‘H’ for the high-frequency mode. The seeding level is indicated with a ‘d’ for deplete or an ‘a’ for abundant.

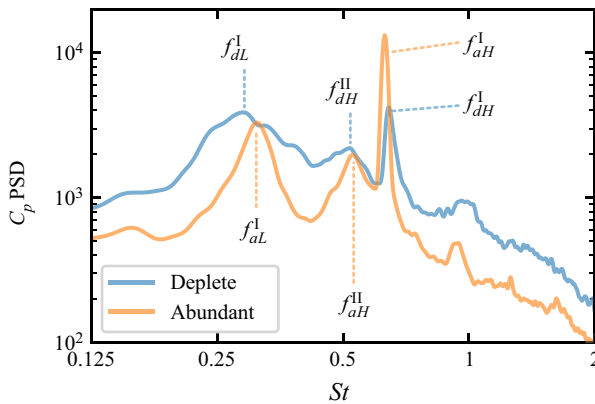


Figure 16. Power spectral density of the pressure signals in regime I.  $\sigma = 0.825$  for the deplete (blue) and  $\sigma = 0.800$  for the abundant (orange) cases. The high-frequency modes from regime II are also indicated.

For  $\sigma < 0.90$ , a bi-modal response commences in both nucleation conditions for which three regimes are apparent with selected  $\sigma$  values labelled I, II and III in figures 14 and 15 with corresponding frequencies for each mode listed in table 1. Similar spectrograms previously derived from a single surface pressure measurement by de Graaf *et al.* (2017) identified attached and detached regimes at higher and lower  $\sigma$  values, respectively. This observation is confirmed with the present higher resolution spectrograms although two sub-regimes, I and II, within the attached regime are apparent, although regime I is limited to a range or band of cavitation numbers of 0.1.

For the deplete case, the regime I band is centred at about  $\sigma = 0.825$  and for the abundant case about  $\sigma = 0.800$ . The PSD for the selected values of  $\sigma = 0.825$  and  $\sigma = 0.800$  in regime I for the deplete and abundant cases, respectively, are compared in figure 16. Here, frequencies are annotated as follows:  $f_{dL}^I$  indicates the deplete (d), low frequency (L), regime I shedding mode, while  $f_{aH}^{II}$  indicates the abundant (a), high frequency (H), regime II shedding mode. The high- and low-frequency modes for the deplete case ( $f_{dH}^I$  and  $f_{dL}^I$ ) are similar in amplitude whereas the high mode for the abundant case is nearly an order of magnitude greater than the low mode. The high modes in both cases are almost the same frequency and strongly narrow band compared with the low modes. The high mode pressures are in-phase indicating axisymmetric shedding with the abundant case showing greater coherence than the deplete. The low mode, expected to be asymmetric, shows less coherence and ambiguous phase with apparent out-of-phase for the deplete and in-phase for the abundant. These observations are reflected in the

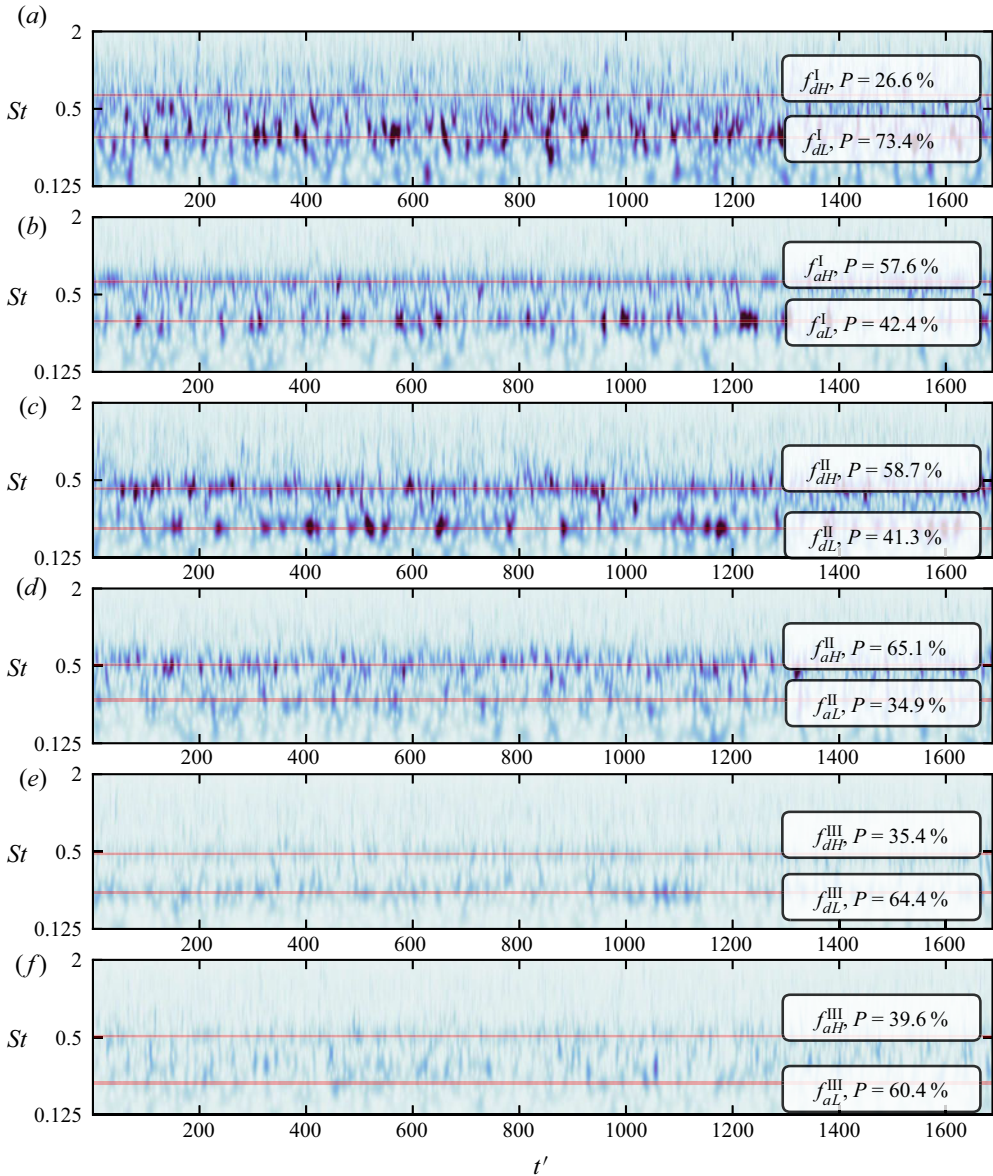


Figure 17. Absolute value of the XWT of the pressure time series between the two sides. The two frequencies of interest for each regime are indicated by the horizontal lines. Rows (a), (c) and (e) are for the deplete configuration, while (b), (d) and (f) are for the abundant. Regime I is shown in figures (a) and (b) with cavitation numbers of 0.825 and 0.800, respectively. Regime II (c,d) is at a cavitation number of 0.750, and regime III (e,f) is 0.600.

XWT plots shown in figure 17. Here, the absolute value of the XWT is given, indicating when the two pressure sensors were simultaneously encountering pressure fluctuations of the same frequency. Qualitatively more low mode than high mode events are evident for the deplete case but conversely more high mode than low mode for the abundant. These observations may be confirmed quantitatively from the durations over which each frequency has the greater amplitude to obtain an overall probability for each mode, as

listed in [figure 17](#). For the deplete case, the low mode has the dominant probability of 73 % and, for the abundant case, the high mode is dominant with a probability of 57.6 %. The unexpected in-phase CPSD result for the abundant case may be attributable to the lack of events due to the prevalence of the high mode combined with random circumference variation of the asymmetric shedding being unresolved from only two correlated pressure measurements.

These observations can be further explored using the high-speed imaging directly and via extracted space–time plots from a horizontal line through the centre of the sphere. Unfortunately, high-speed imaging was only taken for  $\sigma = 0.800$  and not at  $\sigma = 0.825$  so that the regime I deplete modes could be studied in isolation. Examples of the high mode have been identified in the imaging at  $\sigma = 0.800$  along with the regime II modes where the low mode is dominant. Space–time plots for the deplete and abundant cases at  $\sigma = 0.800$  are shown in [figure 18](#) with coloured shaded periods indicating examples of several modes in regimes I and II as indicated. The frequencies for each modes were determined from the corresponding pressure time series using the wavelet transform. Movies for each mode as indicated are provided in the online material for  $\sigma = 0.800$  (movies 2 to 7). For the abundant case, there is a prevalence of highly coherent short period shedding events whereas, for the deplete case, there are fewer longer events. From the high-speed imaging it can be seen that cavity lengths just become long enough for coupled re-entrant jet and shock phenomena to form in both nucleation conditions. For  $\sigma = 0.800$ , the shockwaves are triggered by re-entrant jet formation and can be seen to propagate upstream unlike at  $\sigma = 0.900$  where there were no re-entrant jets and the shock front is stalled not propagating upstream.

The high-speed imaging (available online as movie 7) shows the abundant high mode shedding to be due to coupled re-entrant jet/shockwave phenomena with a high degree of axisymmetry driven or enhanced by the continuous supply of activated nuclei around the sphere periphery. The order of magnitude greater PSD amplitude of the abundant high mode compared with the deplete high mode is most likely attributable to this axisymmetric stabilisation with the abundant nuclei supply. Correspondingly this would also explain the greater probability of the abundant high mode and perhaps also a contributing factor to the unresolved CPSD phase for the suppressed low mode. The imaging also appears to show the low mode shedding to occur with only slight asymmetries in cavity length due to the nucleation promoting axisymmetric growth. Examination of the imaging and unsteady surface pressure for temporal segments at the low mode frequency do show oblique vortical structures in the sphere wake but in-phase pressures suggest on-body cavity growth is symmetric and instabilities develop after detachment. Again, these may be further contributing factors to the unresolved phase angles between the near and far unsteady pressures. The axisymmetric forcing of the abundant nucleation may also explain the regime I occurring at a slightly lower cavitation number than for the deplete case.

From the imaging (available online as movie 4), the deplete high mode appears due to local three-dimensional re-entrant jets and shockwaves that lead to early breakup of the growing cavities, resulting in much shorter cavity lengths and more frequent events compared with the cavity lengths that form during more coherent events that occur in regime II.

In summary, for both nucleation cases in regime I, cavity lengths become just long enough for coupled re-entrant jet and shockwave formation to drive weakly bi-modal shedding with the high-frequency, axisymmetric mode dominating. For the abundant case, the nuclei supply amplifies or forces axisymmetric cavity growth and shedding. The high-frequency modes in both nucleation cases have essentially equal frequencies higher

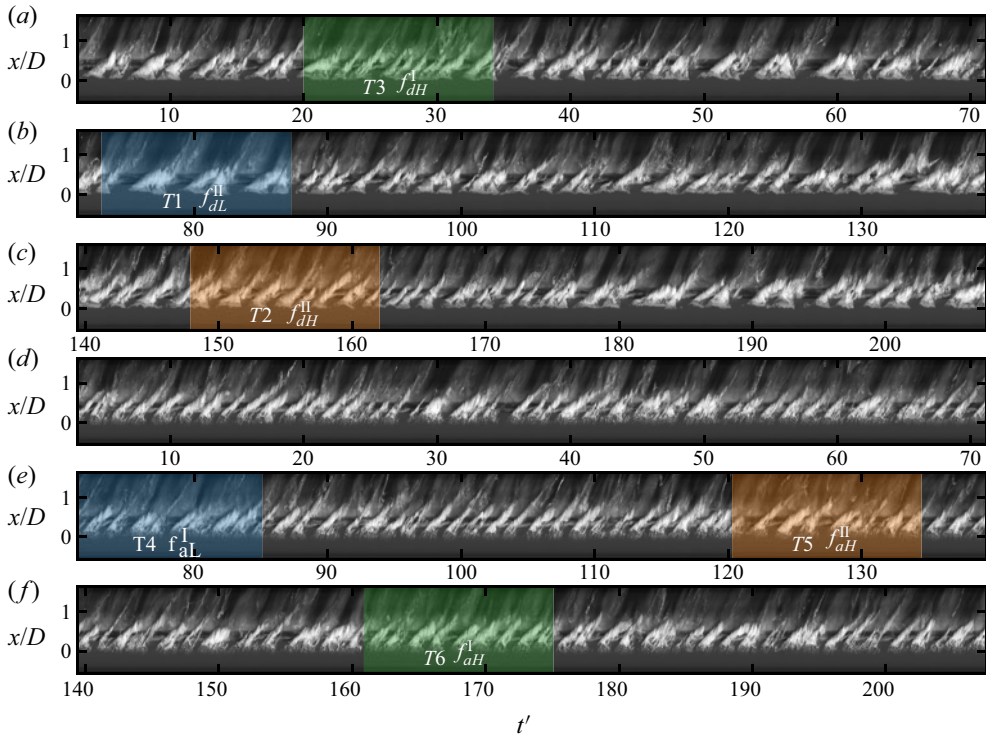


Figure 18. Spatio-temporal maps extracted from a horizontal line through the centre of the sphere of the cavity shedding for the deplete (*a–c*) and abundant (*d–f*) cases at  $\sigma = 0.8$ . The duration of each row is 1 s. The flow is from bottom to top. Structures moving downstream have a positive gradient, and the upstream propagation of shockwaves have a negative gradient. Events at three distinct time scales are evident in the deplete case, while shorter modes are more dominant for the abundant flow. The segments highlighted in blue, orange and green are extracted in figure 24 and correspond to regime II low, regime II high and regime I high, respectively. For the abundant case, the segments highlighted correspond to regime I low, II high and I high, respectively. Videos of these segments are available online as supplementary material and movies 2–7.

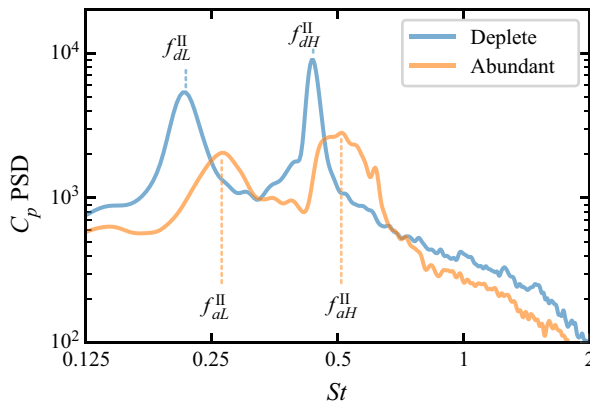


Figure 19. Power spectral density of the pressure signals in regime II. Here  $\sigma = 0.75$  for the deplete (blue) and for the abundant (orange) cases.

### Nucleation effects on cavitation about a sphere

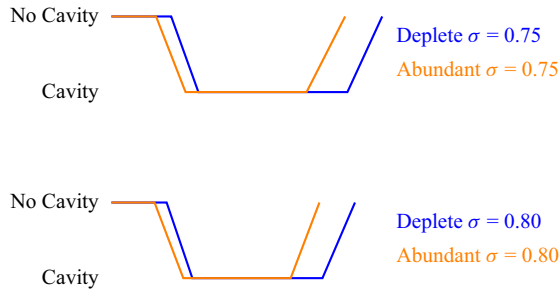


Figure 20. Schematic showing the average cavity shedding cycle for two cavitation numbers and each seeding configuration. The growth and shrinking phases are similar duration, but the time with and without the cavity present are shorter for the abundant cases.

Segment	$\sigma = 0.75$		$\sigma = 0.80$	
	Deplete	Abundant	Deplete	Abundant
No cavitation	7.9	5.9	7.3	5.7
Pressure reducing	3.6	3.9	3.4	3.8
Cavity present	19.7	16.0	17.2	14.2
Pressure increasing	4.6	5.1	4.3	3.8
Total	35.9	30.9	32.3	28.7

Table 2. Average duration of each segment of the cavity shedding cycle for each nuclei concentration. The times are in milliseconds.

than those for regime II due to similar cavity growth rates but shorter lengths at which destabilisation occurs.

Regime II shows strong bi-modal response in both nucleation cases (figure 14) with the deplete case having much greater PSD amplitudes in both modes than the abundant case. From figure 15 it can be seen that the high and low modes are highly coherent in- and out-of-phase, respectively. The low mode for the abundant case appears much weaker, as shown in figure 14, although a clearer comparison of the PSD at  $\sigma = 0.75$  is made in figure 19. The high modes in both nucleation cases are of greater amplitude than the low modes. The amplitudes of each mode for the deplete case are nearly an order of magnitude greater than the corresponding modes for the abundant case. These differences in amplitude correspond to those discussed above for the standard deviation across the attached regime attributed to differences in void fraction and coherence for each nucleation condition. It can also be seen from figure 19 that both modes for the abundant case occur at higher frequencies than the deplete modes. These differences can be explained from basic statistical analysis of the unsteady pressure waveforms. The pressure signals may be segregated into periods of high and low, corresponding to with and without a cavity present, as well as periods of rising and falling pressure, as shown schematically in figure 20 with the periods listed in table 2. These data show that the periods of pressure rise and fall, or cavity growth and shockwave/collapse phases are similar for each nucleation condition. The frequency differences are mostly attributable to periods where there is no cavity, or between a shedding event and re-nucleation, and the period for which a cavity is present. These observations are reflected, and may be seen qualitatively, in the space-time images for the deplete and abundant cases shown in figure 18. It is evident that there are

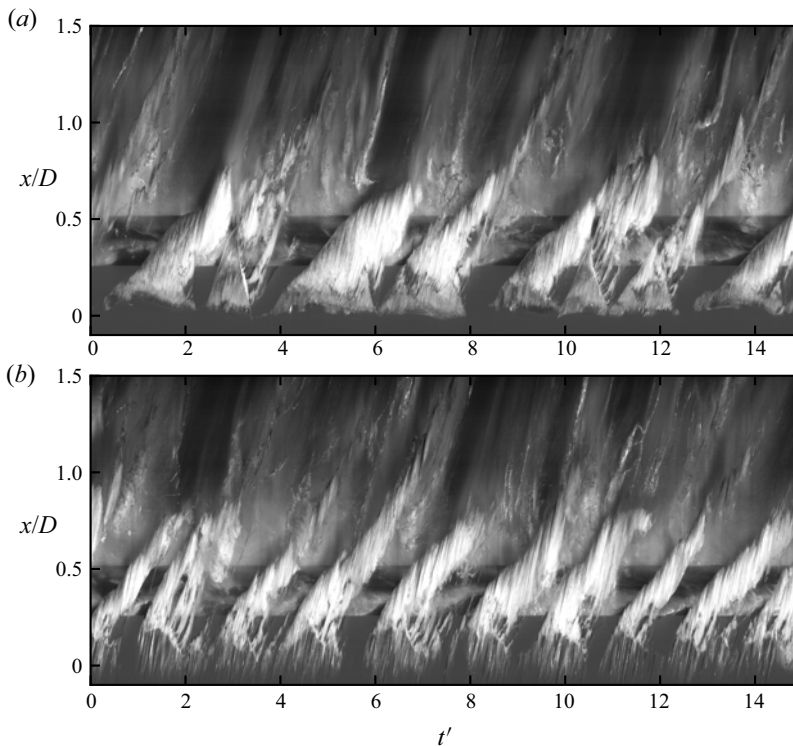


Figure 21. Spatio-temporal map extracted from a horizontal line through the centre of the sphere of the cavitation extent for a cavitation number of 0.800. The (a) figure is deplete of nuclei, while the (b) is abundantly seeded. The flow is from bottom to top. Structures advecting downstream have a positive gradient, and the upstream propagation of shockwaves have a negative gradient.

far fewer shedding events in the deplete case than in the abundant and that the duration where the cavity is either present or not present are greater than those in the abundant case. Larger-scale segments of the space–time plots from figure 18 presented in figure 21 comparing equal periods of time for deplete and abundant cases show these differences more clearly. It can also be seen from figures 18 and 21 that most of the longer events in the deplete case are two successive or coupled events with a short duration of extinction between them. It will be shown that these events correspond with the regime II low mode. Similar observations can also be made from the XWT plots shown in figure 17 for  $\sigma = 0.75$ . The probability or prevalence of the low mode is greater for the deplete case than the abundant. Differences in the duration statistics described for when there is and is not a cavity present and overall differences in the modal frequencies may then be attributable to the effects of nucleation. As argued for regime I, the continuous supply of nuclei for the abundant case not only shortens the periods between shed cavities but also drives the high axisymmetric mode preferentially over the low asymmetric mode.

As noted above, the space–time plots shown in figures 18 and 21 for the deplete case show regular occurrence of paired shedding events of which an example is shown in figure 22. An initial cavity grows and a re-entrant jet and shockwave form detaching the first cloud that, as can be seen, is not advected downstream. A second cavity then develops followed by a re-entrant jet and shockwave but in this case the detached cloud may be seen to be advected downstream. Space–time segments of the synchronised dual high-speed photography (video is available online as movie 8) of the near and far side of the sphere are

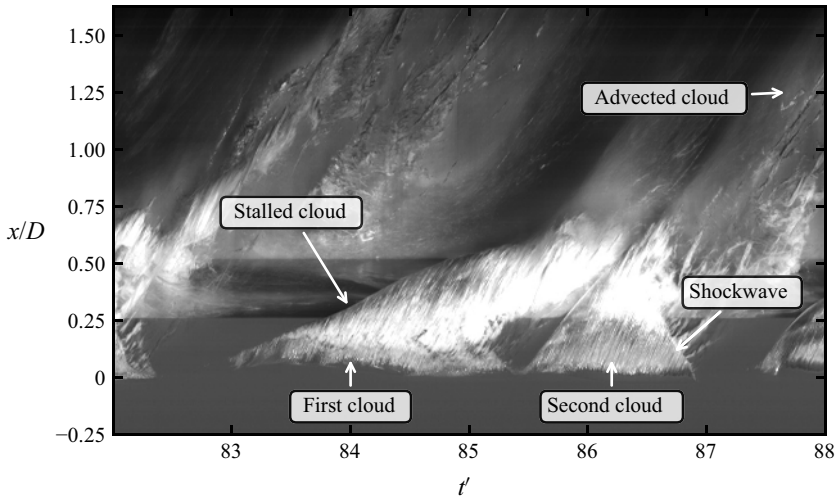


Figure 22. Spatio-temporal map extracted from a horizontal line through the centre of the sphere of the cavitation showing a single regime II, low-frequency shedding event, consisting of two cloud cavities. The first cavity grows before stalling near the end of the sphere. The second cavity grows and its shockwave extinguishes the cavity. The cavitation number is 0.800 and there is no additional seeding.

shown in figure 23. These images show a sequence of paired shedding events on each side qualitatively to be out-of-phase suggesting these events do correspond with the regime II low mode. These images are typical, as per much longer space–time sequences, in showing that the first event is not advected downstream whereas the second is and that these paired events tend to occur in clusters.

To confirm this observation, space–time sequences and surface pressure time series may be locally analysed using the CWT to discern the features corresponding to each mode, as shown in figure 24 for the deplete case at  $\sigma = 0.8$ . In this figure three sequences of equal duration (a–c) have been selected from figure 18, as indicated. Wavelet transform analysis of these sequences show the frequencies to correspond with those for the regime II low mode, regime II high mode and regime I high mode, respectively. The near- and far-side unsteady surface pressures acquired simultaneously with the high-speed imaging are shown in the second row of plots. The CWT and XWT amplitudes are shown in the third and fourth row plots, respectively, and the horizontal lines show the frequencies of interest. The arrows in the CWT plots indicate the phase and the real component of the XWT is shown in the right-hand side plot. Positive values of the XWT real component indicate nominally in-phase and negative out-of-phase, and the magnitude the degree of coherence. The real component for the regime II low mode is negative indicating out-of-phase shedding with a relatively larger amplitude than the other modes. The real components for the regime I and II high modes are positive indicating in-phase shedding but with relatively less coherence compared with the regime II low mode. The greatest response for regime II in the deplete case occurs at about  $\sigma = 0.75$  for which a similar analysis as above has been carried out, as shown in figure 25. Selected temporal sequences with frequencies matching the low and high modes show corresponding out-of-phase and in-phase real components, respectively, with greater coherence than the  $\sigma = 0.8$  results.

The segments of high-speed imaging identified from the wavelet transform analyses to have frequencies corresponding to the regime II low mode may be analysed to gain insights into the topology of this asymmetric mode. High-speed imaging of the regime

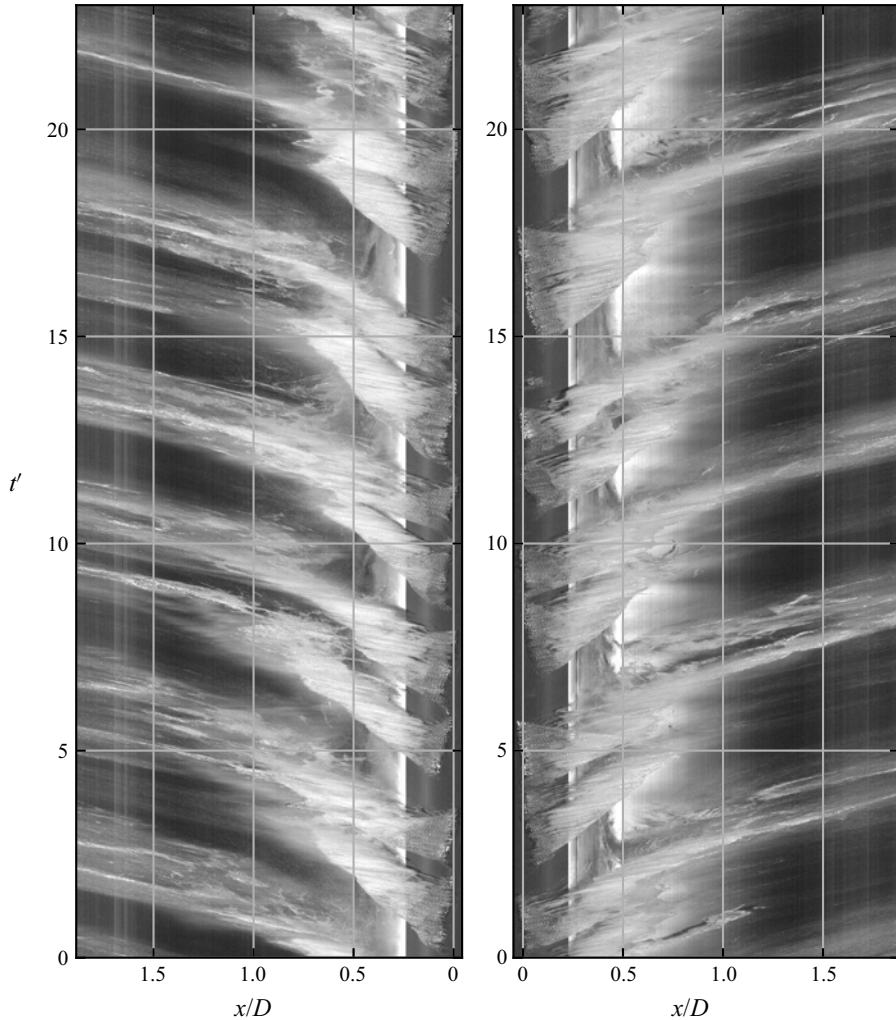


Figure 23. Spatio-temporal map extracted from a horizontal line through the centre of the sphere showing low-frequency regime II shedding from both sides of the sphere. The left column is the near side, while the right column is the far side. Flow is from right to left for the near-side, and left to right for the far-side. The long-duration shedding events are out-of-phase between the two sides. The cavitation number is 0.800 and the flow is depleted of nuclei. The corresponding video of this sequence is available as supplementary material movie 8.

II low mode for the space–time segments shown in figures 21 and 23 are provided in the online material as movies 2 and 8, respectively, and annotated in movie 9. In both these movies a sequence of oblique vortices shedding alternatively from nominally diametrically opposing sides of the sphere can be seen. That is, as can also be seen, the planar symmetry has no preferred azimuthal orientation and may temporally vary between events or clusters of events. The sequence of shedding events in movie 2 has shedding with a nominally horizontal plane of symmetry whereas movie 8 has an oblique plane of symmetry. In both cases cavity growth and subsequent re-entrant jet and shockwave formation are asymmetric resulting in oblique detachment of the shed cavity. The shed vortical rings are distorted or stretched with downstream advection forming classical hairpin shapes with the heads of

Nucleation effects on cavitation about a sphere

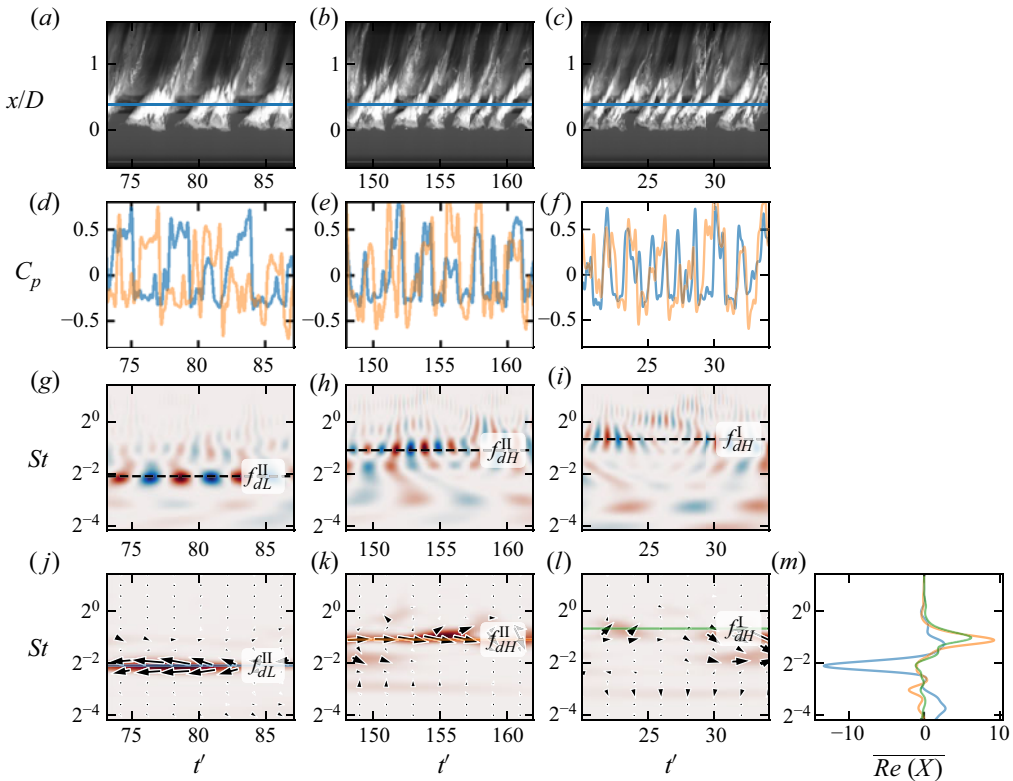


Figure 24. The spatio-temporal map from a horizontal line through the centre of the sphere of cloud cavity position (*a–c*) for the nuclei deplete case at  $\sigma = 0.800$ . These time series were selected to exemplify when each of the three frequencies,  $f_{dL}^{II}$  (*a,d,g,j*),  $f_{dH}^{II}$  (*b,e,h,k*) and  $f_{dH}^I$  (*c,f,i,l*) were dominant. The spatio-temporal map has a horizontal blue line indicating the downstream location of the pressure tap. Sample time series (*d,e,f*) of the pressure coefficient for the near (blue) and far (orange) pressure sensors. The filled contours (*g,h,i*) are the real value of the wavelet transform of the near pressure signal and in (*j*), (*k*) and (*l*) are the XWT between the two sides of the sphere. The arrows indicate the phase difference with an arrow to the right indicating zero phase while an arrow to the left is  $\pi$  out-of-phase. The horizontal lines indicate the frequency of interest and figure *m* is the time average of the real component of the XWT for each of the three frequencies. The time-axis scale is constant across the samples and the duration is 0.2 s for each. These segments are indicated in [figure 18](#).

successive events on diametrically opposing sides of the sphere. The connectivity between each hairpin head and the legs of the previously shed hairpin may also be seen.

From these observations the paired events evident in the space–time plots can be explained. As noted above, the space–time segments in [figures 21](#) and [23](#) show paired events characterised by the first shedding event not showing downstream advection whereas the second does. The paired shedding is also characterised with an interval of cavity extinction between them typically shorter than those separating the pairs. It can be shown from the high-speed imaging that the first shedding event of the pair corresponds to the cavity on the near side receding or rotating about the sphere to the far side while simultaneously on the far side the second cavity of the pair on that side is released. That is, the first event contributes to the junction between each shed hairpin on the far side and the second event shows the downstream advection of the hairpin head shed on the near side.

This topology has been reported on in relation to low Reynolds number shedding about spheres and other axisymmetric bluff bodies in single-phase flows. In liquid–liquid

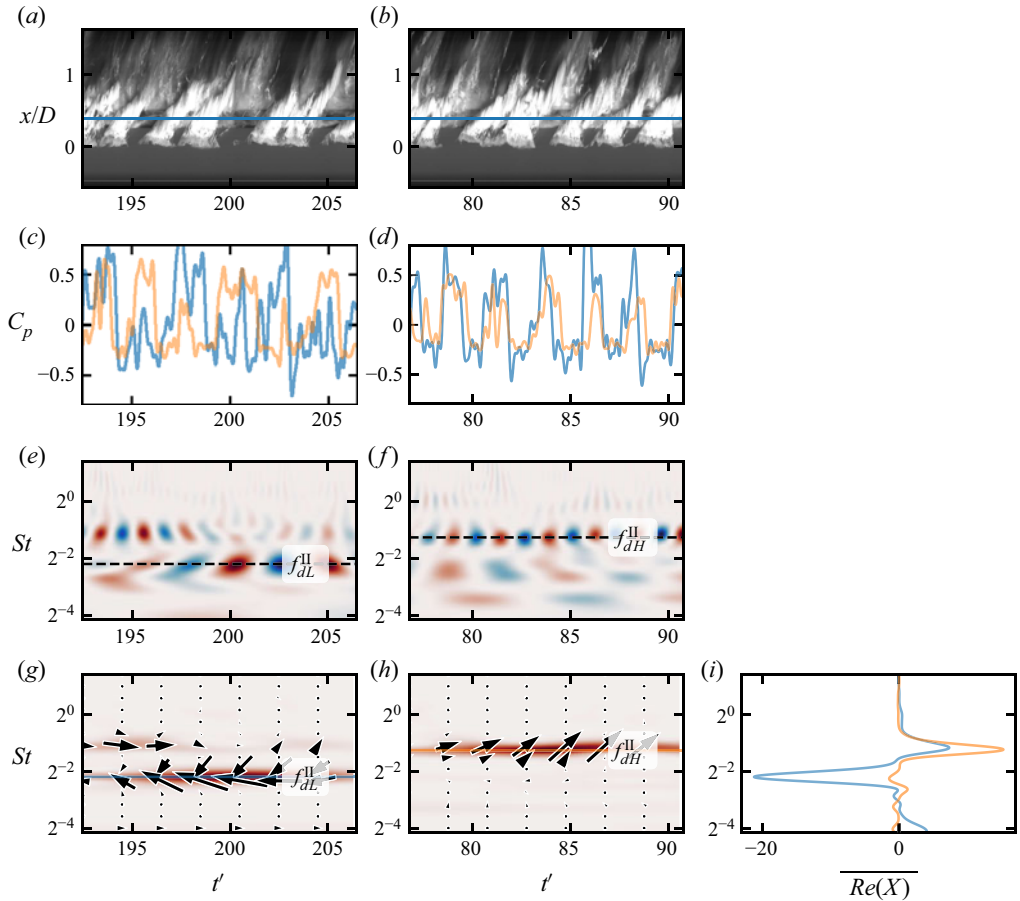


Figure 25. The spatio-temporal map from a horizontal line through the centre of the sphere of cloud cavity position (a,b) for the nuclei deplete case at  $\sigma = 0.750$ . These time series were selected to exemplify when each of the two frequencies,  $f_{dL}^{II}$  (a,c,e,g) and  $f_{dH}^{II}$  (b,d,f,h), were dominant. The spatio-temporal map has a horizontal blue line indicating the downstream location of the pressure tap. Sample time series (c,d) of the pressure coefficient for the near (blue) and far (orange) pressure sensors. The filled contours (e,f) are the real value of the wavelet transform of the near pressure signal and in (g), (h) are the XWT between the two sides of the sphere. The arrows indicate the phase difference with an arrow to the right indicating zero phase while an arrow to the left is  $\pi$  out-of-phase. The horizontal lines indicate the frequency of interest. The time integral of the real value of the XWT is given in i. The time-axis scale is constant across the samples and the duration is 0.2 s for each.

systems (Magarvey & Bishop 1961) using flow visualisation observed alternate vortex shedding from diametrically opposing sides of a descending drop at a Reynolds number of 380. Goldberg & Florsheim (1966) repeated the measurements of Magarvey & Bishop (1961) using solid spheres and other bluff objects and observed regimes with similar modes of alternate hairpin shedding, as described above. Sakamoto & Haniu (1995) report similar results for captive models and provide a summary of observed regimes and modes. Such modes have also been predicted by various computations (e.g. by Johnson & Patel 1999; Sheard, Thompson & Hourigan 2004). Indeed the interesting effect of cavitation to create large-scale von Kármán type shedding at transcritical Reynolds numbers about spheres similar to that in single-phase flows at low Reynolds numbers was noted by Brandner *et al.* (2010).

## Nucleation effects on cavitation about a sphere

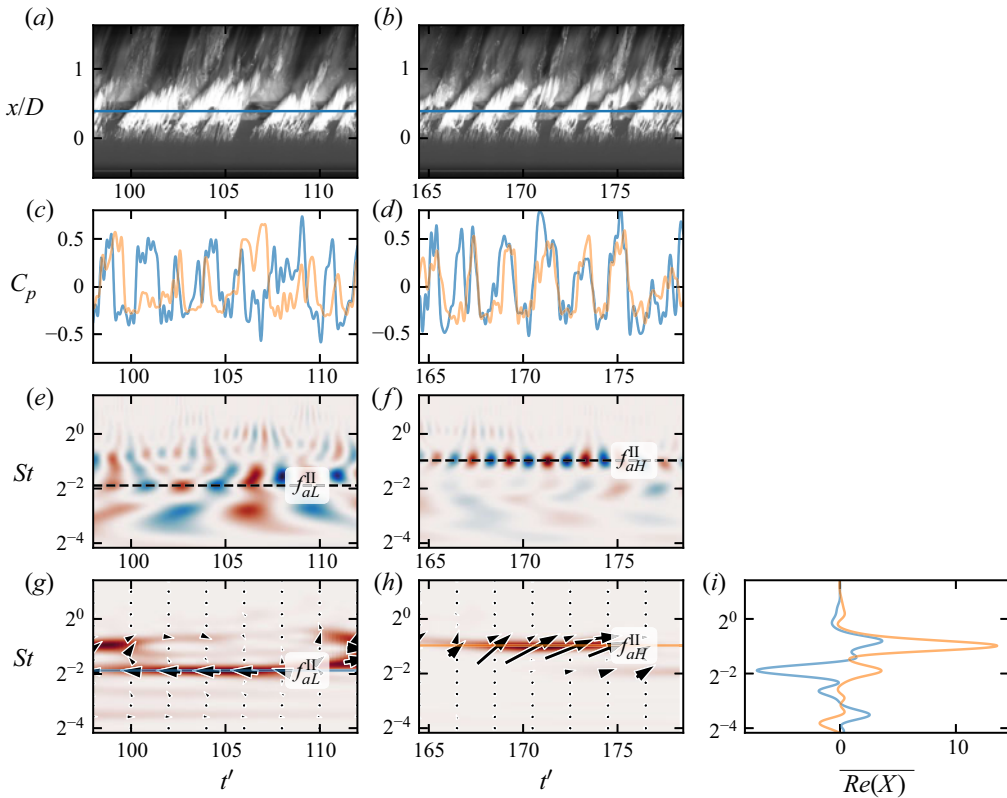


Figure 26. The spatio-temporal map from a horizontal line through the centre of the sphere of cloud cavity position (a,b) for the nuclei abundant case at  $\sigma = 0.750$ . These time series were selected to exemplify when each of the two frequencies,  $f_{aL}^{\text{II}}$  (a,c,e,g) and  $f_{aH}^{\text{II}}$  (b,d,f,h), were dominant. The spatio-temporal map has a horizontal blue line indicating the downstream location of the pressure tap. Sample time series (c,d) of the pressure coefficient for the near (blue) and far (orange) pressure sensors. The filled contours (e,f) are the real value of the wavelet transform of the near pressure signal and in (g), (h) are the XWT between the two sides of the sphere. The arrows indicate the phase difference with an arrow to the right indicating zero phase while an arrow to the left is  $\pi$  out-of-phase. The horizontal lines indicate the frequency of interest. The time integral of the real value of the XWT is given in i. The time-axis scale is constant across the samples and the duration is 0.2 s for each.

As discussed above, for the abundant case in regime II, the supply of activated nuclei increases the frequency of both modes and increases the probability of the high axisymmetric mode compared with the deplete case. The modal topology, however, appears essentially unchanged, although, as the high-speed imaging and data show, shed vortical cavities are not as well defined and of shorter wavelengths than the deplete case due to the effects of discrete bubble activation. The CWT and XWT have been applied to short sequences of the simultaneous surface pressure and high-speed imaging data that correspond to the abundant regime II high and low mode frequencies at  $\sigma = 0.75$ , as shown in figure 26. These data show similar results as for the deplete case (figure 25) in terms of the low mode being out-of-phase and the high mode in-phase. Although the high mode shows greater coherence and the low mode less in the abundant case than for the deplete case, presumably due to the nucleation effects enhancing the high mode, a large number of shedding cycles would need to be analysed to confirm this observation.

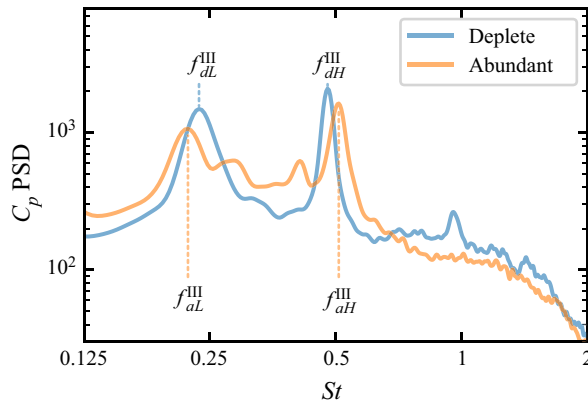


Figure 27. Power spectral density of the pressure signals in regime III ( $\sigma = 0.600$ ) for the deplete (blue) and for the abundant (orange) cases.

In regime III, bi-modal shedding continues but with reduced amplitude and an initial step increase in frequency associated with the transition from attached to detached shedding, as can be seen in figure 14. de Graaf *et al.* (2017) showed this initial step increase in frequency to be the result of greater cavity growth rates once detached despite greater cavity lengths. The PSD spectrograms (figure 14) and XWT (figure 17) show the bi-modal behaviour but at reduced amplitudes compared with regimes I and II. The CPSD shows inconsistent phase depending on both the cavitation number and the nucleation condition possibly attributable to both low amplitudes and insufficient data. A direct comparison of the PSD for each nucleation case at  $\sigma = 0.6$  is shown in figure 27. Few differences are apparent with low and high modes having similar frequencies and a slight reduction in amplitude for both modes between deplete and abundant cases. This confirms the earlier observation from the standard deviation of the surface pressures that the cavity volumes are sufficiently large that differences in nucleation have little effect on the shedding behaviour. Observation of the high-speed imaging also confirms this result. The low-frequency mode cavity topology is uncertain due to cavity lengths being greater than the camera field of view.

#### 4. Conclusions

The influence of deplete and abundant nucleation conditions on cloud cavitation about a sphere at transcritical Reynolds numbers has been investigated from inception through to supercavitation. In both nucleation cases uni-modal shedding occurs at incipient cavitation numbers of about 1.0 to 0.9. Bi-modal shedding develops for cavitation numbers below 0.9 driven by coupled re-entrant jet formation and upstream shockwave propagation. The high-frequency mode is axisymmetric and the low-frequency mode asymmetric. Previous observations of bi-modal shedding occurring in two, attached and detached, regimes are confirmed. Although, two sub-regimes within the attached regime were resolved from high-resolution spectrograms of unsteady surface pressure on two sides of the sphere as a function of cavitation number. The initial regime is limited to a narrow cavitation number band of about 0.1 centred at 0.825 and 0.8 for deplete and abundant cases, respectively. The second attached regime occurs over a larger range of cavitation numbers centred at 0.75 for both nucleation cases. For cavitation numbers below about 0.675, the detached regime begins which transitions to supercavitation with cavitation number reduction.

The modes that occur in each regime are related to the scale of the cavitation relative to that of the sphere and the extent to which each are affected by the driving re-entrant jet and shockwave mechanisms.

For the nuclei deplete case, where no artificial seeding is added to the free stream, cavitation numbers are too high to activate the natural population such that there is effectively no available nuclei. Beyond inception the cavity leading edge or detachment is clearly defined associated with laminar separation of the approaching boundary layer. Instability in the overlying boundary layer controls cavity breakup at incipient cavitation numbers only. As the first bi-modal attached regime occurred in a narrow cavitation number band, where high-speed imaging was not taken, there is uncertainty as to the nature of the asymmetric low mode. However, high-speed imaging at a cavitation number of 0.8 shows local three-dimensional re-entrant jet and shockwave behaviour which is a likely source of initial asymmetry. The second bi-modal attached regime shows the greatest coherence with cavity lengths of the order of the sphere diameter and, hence, the potential for large-scale interactions on opposing sides of the sphere. The low asymmetric mode is shown to be due to alternate shedding of oblique vortices from diametrically opposing sides of the sphere, similar in topology to low Reynolds number shedding about spheres and other axisymmetric bluff bodies in single-phase flows. In the detached regime where cavity lengths are greater than the sphere diameter a similar low mode topology is possible, but imaging at scales greater than the sphere diameter is required for confirmation.

For the nuclei abundant case, the total free-stream polydisperse nuclei concentration is order  $10^7 \text{ m}^{-3}$  with sizes ranging between order 10 to 100  $\mu\text{m}$ . As a result, there are typically a high number of activated nuclei about the sphere such that bubble diameters and inter-bubble spaces are small compared with the sphere diameter. Activated nuclei grow to maximum sizes of about 1 cm at area concentrations of order  $1 \text{ cm}^{-2}$  both of which increase with decreasing cavitation number. Local turbulent flows about the growing activated nuclei break up the laminar boundary layer and cavity volume such that there is no defined detachment line. This effect has the greatest influence at higher cavitation numbers where cavity volumes are relatively small both on small-scale and large-scale instabilities. At incipient cavitation numbers nuclei activations break up the fine-scale interfacial effects such that there is an increase in unsteady pressures in the abundant case compared with the deplete. Nuclei activation rates at high cavitation numbers measured from the high-speed imaging are about an order of magnitude less than those estimated from the measured nuclei population assuming uncoupled inviscid single-phase flow about the sphere. Based on this and other analyses this difference is attributable to the growing activated nuclei reducing the volume of fluid under tension. That is, the rate of nuclei activation has reached saturation such that any increase in nuclei concentration produces no increase in activation rates. This result suggests further experiments are required at lower nuclei concentrations.

The continuous supply of activated nuclei around the sphere periphery in the first bi-modal regime has the effect of driving the high symmetric mode preferentially over the asymmetric low mode compared with the deplete case. For the deplete case, high/low mode probabilities are 27/73 % compared with 58/42 % for the abundant. Examination of high-speed imaging and unsteady surface pressure for temporal segments at the low mode frequency do show oblique vortical structures in the sphere wake but pressures are in-phase suggesting on-body cavity growth is symmetric, due to continuous seeding, and instabilities develop after detachment.

The abundant nucleation in the second bi-modal regime has a similar, but much less effect, as for the first in driving the axisymmetric high mode over the low compared

with the deplete nucleation case. For the deplete case, high/low mode probabilities are 59/41 % compared with 65/35 % for the abundant. This difference between the first and second regimes is presumably due to greater cavity volume and more energetic shedding that occurs in the second regime compared with the first. For the first bi-modal regime, the abundant nucleation had the effect of shifting the cavitation number at which the coherence occurred to a lower value than for the deplete case. Whereas, for the second bi-modal regime, the abundant nucleation had the effect of increasing the frequency of both high and low modes compared with the deplete whilst the cavitation number for maximum coherence remained about the same. The frequency increases of each mode with the abundant nucleation were shown to be due to reduction of both inter-cavity and cavity durations. The abundant low mode topology is essentially the same as for the deplete case but with shorter wavelengths and less definition due to discrete bubble effects.

For the detached regime, where cavity volumes are large compared with the sphere size, instabilities are moved downstream such that differences in nucleation have little effect and unsteady pressures and modal frequencies are essentially the same.

Future work would include more detailed investigation at cavitation numbers at maximum coherence to fully resolve low mode typologies, larger numbers of pressure sensors combined with dual cameras for greater spatio-temporal resolution of modes and intermediate nuclei concentrations between the extremes of the present investigation.

**Supplementary material and movies.** Supplementary material and movies are available at <https://doi.org/10.1017/jfm.2022.511>.

**Acknowledgements.** The authors wish to acknowledge the technical support of Mr R. Wrigley and Mr S. Kent and the assistance of Dr D. Giosio in acquiring the experimental data.

**Funding.** The authors acknowledge the support of the Australian Defence Science and Technology Group.

**Declaration of interests.** The authors report no conflict of interest.

#### Author ORCIDs.

 Paul A. Brandner <https://orcid.org/0000-0002-6721-878X>;

 James A. Venning <https://orcid.org/0000-0002-4097-2168>;

 Bryce W. Pearce <https://orcid.org/0000-0003-2189-5598>.

#### REFERENCES

- ACHENBACH, E. 1972 Experiments on the flow past spheres at very high Reynolds numbers. *J. Fluid Mech.* **54**, 565–575.
- ARAKERI, V.H. 1975 Viscous effects on the position of cavitation separation from smooth bodies. *J. Fluid Mech.* **68** (4), 779–799.
- ARAKERI, V.H. & ACOSTA, A.J. 1973 Viscous effects in the inception of cavitation on axisymmetric bodies. *J. Fluids Engng* **95** (4), 519–527.
- ARNDT, R.E.A. & KELLER, A.P. 1992 Water quality effects on cavitation inception in a trailing vortex. *J. Fluids Engng* **114** (3), 430–438.
- ARNDT, R.E.A. & KELLER, A.P. 2003 A case study of international cooperation: 30 years of collaboration in cavitation research. In *4th ASME–JSME joint Fluids Engineering Summer Meeting*. ASME.
- ARNDT, R.E.A. & MAINES, B.H. 2000 Nucleation and bubble dynamics in vortical flows. *J. Fluids Engng* **122** (3), 488–493.
- BAKIĆ, V. & PERIĆ, M. 2005 Visualization of flow around sphere for Reynolds numbers between 22 000 and 400 000. *Thermophys. Aeromech.* **12** (3), 307–315.
- BEELEN, S. & VAN RIJSBERGEN, M.X. 2018 Bubble screening in lifting flows and its effect on cavitation inception. In *Numerical Towing Tank Symposium (NuTTS) 30th Sept–2nd Oct 2018* (ed. V. Bertram).
- BRANDNER, P.A., LECOFFRE, Y. & WALKER, G.J. 2007a Design considerations in the development of a modern cavitation tunnel. In *16th Australasian Fluid Mechanics Conference*. AFMS.

## Nucleation effects on cavitation about a sphere

- BRANDNER, P.A., VENNING, J.A. & PEARCE, B.W. 2018 Wavelet analysis techniques in cavitating flows. *Philos. Trans. R. Soc. A* **376**, 20170242.
- BRANDNER, P.A., WALKER, G.J., NIEKAMP, P.N. & ANDERSON, B. 2007b An investigation of cloud cavitation about a sphere. In *16th Australasian Fluid Mechanics Conference*, pp. 1392–1398. AFMS.
- BRANDNER, P.A., WALKER, G.J., NIEKAMP, P.N. & ANDERSON, B. 2010 An experimental investigation of cloud cavitation about a sphere. *J. Fluid Mech.* **656**, 147–176.
- BRENNEN, C. 1969 The dynamic balances of dissolved air and heat in natural cavity flows. *J. Fluid Mech.* **37** (1), 115–127.
- BRENNEN, C. 1970 Cavity surface wave patterns and general appearance. *J. Fluid Mech.* **44** (1), 33–49.
- BRENNEN, C.E. 1995 *Cavitation and Bubble Dynamics*. Cambridge University Press.
- BRIANÇON-MARJOLLET, L., FRANC, J.P. & MICHEL, J.M. 1990 Transient bubbles interacting with an attached cavity and the boundary layer. *J. Fluid Mech.* **218**, 355–376.
- BRIANÇON-MARJOLLET, L. & FRÉCHOU, D. 1992 Cavitation in “Le Grand Tunnel Hydrodynamique” (GTH). In *2nd International Symposium on Propeller and Cavitation*, pp. 256–264.
- BRIANÇON-MARJOLLET, L. & MICHEL, J.M. 1990 The hydrodynamic tunnel of I.M.G.: former and recent equipments. *J. Fluids Engng* **112** (3), 338–342.
- CALLENAERE, M., FRANC, J.-P., MICHEL, J.-M. & RIONDET, M. 2001 The cavitation instability induced by the development of a re-entrant jet. *J. Fluid Mech.* **444**, 223–256.
- CHEN, L., ZHANG, L., PENG, X. & SHAO, X. 2019 Influence of water quality on the tip vortex cavitation inception. *Phys. Fluids* **31** (2), 023303.
- CHENG, X., SHAO, X. & ZHANG, L. 2019 The characteristics of unsteady cavitation around a sphere. *Phys. Fluids* **31** (4), 042103.
- DAMASCHKE, N., NOBACH, H. & TROPEA, C. 2002 Optical limits of particle concentration for multi-dimensional particle sizing techniques in fluid mechanics. *Exp. Fluids* **32** (2), 143–152.
- FRANC, J.-P. & MICHEL, J.-M. 2005 *Fundamentals of Cavitation*. Springer Science & Business Media.
- GHAHRAMANI, E., STRÖM, H. & BENSOW, R.E. 2021 Numerical simulation and analysis of multi-scale cavitating flows. *J. Fluid Mech.* **922**, A22.
- GINDROZ, B. & BILLET, M.L. 1998 Influence of the nuclei on the cavitation inception for different types of cavitation on ship propellers. *J. Fluids Engng* **120** (1), 171–178.
- GIOSIO, D., PEARCE, B.W. & BRANDNER, P.A. 2016 Influence of pressure on microbubble production rate in a confined turbulent jet. In *20th Australasian Fluid Mechanics Conference*. AFMS.
- GOLDBURG, A. & FLORSHEIM, B.H. 1966 Transition and strouhal number for the incompressible wake of various bodies. *Phys. Fluids* **9** (1), 45–50.
- DE GRAAF, K.L., BRANDNER, P.A. & PEARCE, B.W. 2017 Spectral content of cloud cavitation about a sphere. *J. Fluid Mech.* **812**, R1.
- DE GRAAF, K.L., PEARCE, B.W. & BRANDNER, P.A. 2016 The influence of nucleation on cloud cavitation about a sphere. In *ISROMAC16 – Sixteenth International Symposium on Transport Phenomena and Dynamics of Rotating Machinery*.
- GRINSTED, A., MOORE, J.C. & JEVREJEVA, S. 2004 Application of the cross wavelet transform and wavelet coherence to geophysical time series. *Nonlinear Process. Geophys.* **11**, 561–566.
- HSIAO, C.-T., MA, J. & CHAHINE, G.L. 2017 Multiscale two-phase flow modeling of sheet and cloud cavitation. *Intl J. Multiphase Flow* **90**, 102–117.
- HSIAO, C.-T., MA, J. & CHAHINE, G.L. 2018 Dynamics of dispersed bubbly flow over a lifting surface: gas diffusion and bubble breakup effects. In *32nd Symposium on Naval Hydrodynamics*, Paper 144. ONR.
- JOHNSON, T.A. & PATEL, V.C. 1999 Flow past a sphere up to a reynolds number of 300. *J. Fluid Mech.* **378**, 19–70.
- KAWAKAMI, D.T., FUJI, A., TSUJIMOTO, Y. & ARNDT, R.E.A. 2008 An assessment of the influence of environmental factors on cavitation instabilities. *J. Fluids Engng* **130** (3), 031303.
- KAWAKAMI, D.T., QIN, Q. & ARNDT, R.E.A. 2003 Can water quality affect the lift dynamics of cavitating hydrofoils? In *Fifth International Symposium on Cavitation – CAV2003*, Paper GS-4-007.
- KHOO, M.T., VENNING, J.A., PEARCE, B.W., TAKAHASHI, K., MORI, T. & BRANDNER, P.A. 2020 Natural nuclei population dynamics in cavitation tunnels. *Exp. Fluids* **61**, 34.
- LECOFFRE, Y. 1999 *Cavitation: Bubble Trackers*. CRC Press.
- LI, C.-Y. & CECCIO, S.L. 1996 Interaction of single travelling bubbles with the boundary layer and attached cavitation. *J. Fluid Mech.* **322**, 329–353.
- LINDGREN, H. & JOHNSON, C.A. 1966 Cavitation inception on head forms - ITTC comparative experiments. In *Eleventh International Towing Tank Conference*, pp. 219–232. ITTC.
- LIU, Z., KUHN DE CHIZELLE, Y. & BRENNEN, C.E. 1993 Cavitation event rates and nuclei distributions. In *ASME Symposium on Cavitation Inception, FED-Vol. 177*, pp. 13–23. ASME.

- MAGARVEY, R.H. & BISHOP, R.L. 1961 Wakes in liquid-liquid systems. *Phys. Fluids* **4** (7), 800–805.
- PAUL, R.A., VENNING, J.A. & BRANDNER, P.A. 2021 Nuclei transport about a sphere. In *Eleventh International Symposium on Cavitation – CAV2021*.
- PENDAR, M.-R. & ROOHI, E. 2018 Cavitation characteristics around a sphere: an LES investigation. *Intl J. Multiphase Flow* **98**, 1–23.
- RAM, O., AGARWAL, K. & KATZ, J. 2020 On the mechanisms that sustain the inception of attached cavitation. *J. Fluid Mech.* **901**, R4.
- RUSSELL, P.S., BARBACA, L., VENNING, J.A., PEARCE, B.W. & BRANDNER, P.A. 2020a Measurement of nuclei seeding in hydrodynamic test facilities. *Exp. Fluids* **61**, 79.
- RUSSELL, P. & BRANDNER, P. 2021 Nucleation dynamics in cloud cavitation. In *Eleventh International Symposium on Cavitation – CAV2021*.
- RUSSELL, P., VENNING, J., PEARCE, B.W. & BRANDNER, P.A. 2020b Calibration of Mie scattering imaging for microbubble measurement in hydrodynamic test facilities. *Exp. Fluids* **61**, 93.
- SAKAMOTO, H. & HANIU, H. 1990 A study on vortex shedding from spheres in a uniform flow. *J. Fluids Engng* **112**, 386–392.
- SAKAMOTO, H. & HANIU, H. 1995 The formation mechanism and shedding frequency of vortices from a sphere in uniform shear flow. *J. Fluid Mech.* **287**, 151–171.
- SCHMIDT, S.J., SEZAL, I.H., SCHNERR, G.H. & THALHAMER, M. 2008 Numerical analysis of shock dynamics for detection of erosion sensitive areas in complex 3-D flows. In *WIMRC Cavitation Forum 2008 – Cavitation: Turbo-Machinery & Medical Applications*, pp. 107–120. Warwick IMRC.
- SHEARD, G.J., THOMPSON, M.C. & HOURIGAN, K. 2004 From spheres to circular cylinders: non-axisymmetric transitions in the flow past rings. *J. Fluid Mech.* **506**, 45–78.
- TASSIN LEGER, A., BERNAL, L.P. & CECCIO, S.L. 1998 Examination of the flow near the leading edge of attached cavitation: part 2. Incipient breakdown of two-dimensional and axisymmetric cavities. *J. Fluid Mech.* **376**, 91–113.
- TASSIN LEGER, A. & CECCIO, S.L. 1998 Examination of the flow near the leading edge of attached cavitation: part 1. Detachment of two-dimensional and axisymmetric cavities. *J. Fluid Mech.* **376**, 61–90.
- TORRENCE, C. & COMPO, G.P. 1998 A practical guide to wavelet analysis. *Bull. Am. Meteorol. Soc.* **79** (1), 61–78.
- VENNING, J.A., GIOSIO, D.R., PEARCE, B.W. & BRANDNER, P.A. 2018a Global mode visualisation in cavitating flows. In *Tenth International Symposium on Cavitation – CAV2018*, pp. 485–490. ASME Press.
- VENNING, J., GIOSIO, D., SMITH, S., PEARCE, B. & BRANDNER, P. 2018b The influence of nucleation on the spectral content of cloud cavitation about a hydrofoil. In *Tenth International Symposium on Cavitation – CAV2018*, pp. 1025–1030. ASME.
- VENNING, J.A., KHOO, M.T., PEARCE, B.W. & BRANDNER, P.A. 2018c Background nuclei measurements and implications for cavitation inception in hydrodynamic test facilities. *Exp. Fluids* **59** (4), 71.
- VENNING, J.A., PEARCE, B.W. & BRANDNER, P.A. 2021 Dual-camera mode visualization of cavitating flows. In *11th International Symposium on Cavitation – CAV2021*.
- VENNING, J., SMITH, S., BRANDNER, P., GIOSIO, D. & PEARCE, B. 2017 The influence of nuclei content on cloud cavitation about a hydrofoil. In *Seventeenth International Symposium on Transport Phenomena and Dynamics of Rotating Machinery – ISROMAC17*.
- WEITENDORF, E.-A. 1981 Cavitation phenomena, propeller excited hull pressure amplitudes and cavitation scale effect. *Ocean Engng* **8** (5), 517–539.
- WELCH, P. 1967 The use of fast Fourier transform for the estimation of power spectra: a method based on time averaging over short, modified periodograms. *IEEE Trans. Audio Electroacoust.* **15** (2), 70–73.